Dynamics of laser ablation at the early stage during and after ultrashort pulse

You may also be interested in:

Adiabatic approximations for electrons interacting with ultrashort high-frequency laser pulses
Koudai Toyota, Ulf Saalmann and Jan M Rost

Blistering of film from substrate after action of ultrashort laser pulse
N A Inogamov, V V Zhakhovsky, V A Khokhlov et al.

Simulation of femtosecond pulsed laser ablation of metals
R V Davydov and V I Antonov

Photoionization of Rydberg States by Ultrashort Wavelet Pulses
S Yu Svita and V A Astapenko

Optical emission spectroscopy of plasma produced by laser ablation of iron sulfide
S Karatodorov, V Mihailov, T Kenek et al.

Fabrication of a microlens array in BK7 through laser ablation and thermal treatment techniques
M Blanco, D Nieto and M T Flores-Arias

Double ionization of molecule H2 in intense ultrashort laser fields
Thu-Thuy Le and Ngoc-Ty Nguyen

Dynamics of laser ablation at the early stage during and after ultrashort pulse

D K Ilnitsky[1,2]**, V A Khokhlov**[2]**, V V Zhakhovsky**[1,2]**, Yu V Petrov**[2]**, K P Migdal**[1,2]** and N A Inogamov**[1,2]

[1] Dukhov Research Institute of Automatics (VNIIA), Sushchevskaya 22, Moscow 127055, Russia
[2] Landau Institute for Theoretical Physics of the Russian Academy of Scienses, Akademika Semenova 1a, Chernogolovka, Moscow Region 142432, Russia

E-mail: `nailinogamov@gmail.com`

Abstract. Study of material flow in two-temperature states is needed for a fundamental understanding the physics of femtosecond laser ablation. To explore phenomena at a very early stage of laser action on a metallic target our in-house two-temperature hydrodynamics code is used here. The early stage covers duration of laser pulse with next first few picoseconds. We draw attention to the difference in behavior at this stage between the cases: (i) of an ultrathin film (thickness of order of skin depth d_{skin} or less), (ii) thin films (thickness of a film is 4–7 of d_{skin} for gold), and (iii) bulk targets (more than $10d_{\text{skin}}$ for gold). We demonstrate that these differences follow from a competition among conductive cooling of laser excited electrons in a skin layer, electron-ion coupling, and hydrodynamics of unloading caused by excess of pressure of excited free electrons. Conductive cooling of the skin needs a heat sink, which is performed by the cold material outside the skin. Such sink is unavailable in the ultrathin films.

1. Introduction

Studies of femtosecond laser ablation are important because, first, these lasers are relatively cheap and now are wide spread, and, second, there are many scientific and industrial applications where they are used. There are a number of important studies devoted to this theme. These papers treat or self-reflection at rather high intensities [1–3], or reflection of a probe pulse in pump-probe experiments [3–5], or consider hydrodynamics of shock waves generated by a laser pulse [6–9], or study thermomechanical ablation [10, 11]. For bulk targets, this type of ablation starts late in time, definitely later than the few first picoseconds. Thermomechanical ablation begins from nucleation of voids at significant depth $\sim d_T$ under a vacuum boundary. This fact relates to the case of a bulk target when thickness of a target d_f is large $d_f \gg d_T$. The scale d_T is thickness of a heat affected zone. It is created during the two-temperature (2T) stage when electron heat conduction has enhanced values [12]. There is supersonic expansion of heat from a skin layer to the bulk of a target at the 2T stage. The rate of expansion of heat inside metal is defined by electron Fermi velocities. Acoustic time scale $t_s = d_T/c_s$ gives duration of the time interval between arrival of a pump pulse and nucleation.

Below we consider a gold film on a glass substrate. Thickness of a film analyzed in our paper is $d_f = 100$ nm. Thickness of a heat affected zone in bulk gold is $d_T = 150 - 200$ nm [13]. Our

film is thinner $d_f < d_T$ than thickness of a heat affected zone. Thus, a film is heated fast and a thermal energy distribution is approximately homogeneous across a film.

Thermomechanical ablation of a homogeneously heated freestanding film is studied well [10, 14, 15]. Slightly above the ablation threshold the film disrupts in its middle plane to two halves. The case with a thin gold film $d_f < d_T$ on a glass substrate has been considered in papers [16, 17]. This case is important for our work. It was shown [16, 17], that the situation with a gold film on a glass is similar to the case of a freestanding film, because acoustic impedance of glass is 6-7 times smaller than acoustic impedance of gold. Presence of glass does situation with a homogeneously heated film slightly asymmetric relative to the middle plane of a film.

Let us say few words about thermomechanical ablation. Unloading into vacuum of an infinitely large homogeneously pressurized semi-space proceeds with limited velocities, flow is self-similar, and there is a fan of the straight characteristics outgoing from the spatiotemporal point $x = 0$, $t = 0$; here we neglect very small duration of a pump pulse, thus the instant $t = 0$ corresponds to arrival of a pump to a surface. The flow with a fan is called a centered rarefaction wave. This is a solution of equations of hydrodynamics corresponding to the decay of jump of parameters (e.g., pressure) between two homogeneous semi-spaces. In this flow the decelerations of material particles and tensile stresses are absent: there are only accelerations of Lagrangian particles up to limiting velocity. The particles achieved this velocity form a plateau [18, 19]. Pressure at plateau equals to pressure of vacuum.

But if the pressurized region is limited in its thickness then deceleration and tensile stress appear. The spatial limitation of a pressurized layer is in a form of finite depth d_T of a heat affected and therefore pressurized surface layer of a semi-space or in a form of a thin film $d_f < d_T$. Some interval of time after excitation by a pump is necessary to achieve a maximum absolute value of a tensile stress. This temporal interval is $\sim d_T/c$ for a bulk target and $\sim d_f/c$ for a thin film; here c is speed of sound. At the thermomechanical ablation threshold, the maximum tensile stress overcomes the material strength, thus nucleation begins. Merging of nuclei causes spallation [10, 11, 20] called thermomechanical ablation inside laser community.

Depth where the nucleation starts is of the order of d_T or d_f for bulk and film targets respectively. This depth defines thickness of a spallation plate. Near ablation threshold this thickness is 70–100 nm for a bulk gold [21] and 40–50 nm for a 100 nm film [17]. Below we show that a much thinner spallation plate also exists.

This is the main idea of the paper. In the classical picture of thermomechanical ablation the spallation follows from a *spatial* inhomogeneity d_T or d_f of a pressurized layer. Contrary to this particular *spatial* source of spallation, the *temporal* factor causes ablation in our new, "non-classical" way to spallation. This second type, "non-classical" electron pressure driven, time dependent ablation is thermomechanical one, as the first type is. It appears thanks to force action of electron pressure increased as a result of heating of electrons [22, 23]. The dynamic effect of electron pressure sharply, during the ultrashort pulse, accelerates the vacuum boundary to finite expansion velocity.

Ablation thresholds for the first and the second type break off are different. It is plausible that the second one is lower. Two ablation thresholds corresponding to early and late time ablations were described in papers [24–26]. These works are based on molecular dynamics (MD) simulation combined with the two-temperature (2T) model which includes not only 2T thermal terms (as in [11]) but also dynamic influence of the excited electrons. The two 2T thermal terms are connected with electron heat conduction and with electron-ion energy exchange, while the dynamic influence according to [24–26] has two factors.

One of these factors is the change of pressure as a result of excitation of electrons at fixed volume. The second factor is the additional change of pressure due to pressure of free electrons. A bulk target has been considered in papers [24–26]. Below we will concentrate on the second type break off for the 100 nm film. It takes place rather early in time, therefore the mechanical

conditions at the opposite side of a film (the rear-side boundary) are not significant (are glass or vacuum placed there); the frontal and the rear-side boundaries do not have time to communicate through sound (but they communicate through supersonic 2T electron thermal heat transfer usually called ballistic transport). The sense of the second type is connected with fast drop down of electron internal energy in a skin-layer. This drop is possible thanks to powerful electron conduction if there is a cold volume contacting with a skin. The electron subsystem of cold volume plays a role of a bulk cooler accepting energy flowing from a skin. Thermal energy flows very fast (faster than speed of sound [12]) along electron subsystem during 2T stage. Therefore the thermal contact between a film thinner than d_T and support becomes important if the support is made from highly conductive material, e.g., crystalline silicon. In our case the supporting substrate is a glass. It is weakly heat conducting. Thus we put the condition of thermal insulation at the rear-side.

The paper is constructed as the following sequence of the connected parts. First of all in section 2 "Thermal fluxes" we pay attention to the interplay of thermal powers and fluxes during the first picoseconds. After that in section 3 "Two-temperature flow" we consider particular 2T-HD simulations to understand the electron fluxes and the electron temperature dependencies on space and time near the vacuum surface. We are interested to consider a layer which will be covered by a hydrodynamic rarefaction wave during the first picoseconds.

There is significant deceleration of the vacuum boundary during the first picoseconds for the weak electron-ion energy exchange rates. The deceleration is caused by the conduction cooling of electron subsystem of a skin layer and the corresponding drop of electron pressure supporting expansion. The deceleration appears under action of negative total pressure inside the rarefaction wave. Stretching of matter results in break off above the certain limit of absolute value of negative pressure. Dynamics of expansion in the spatially isothermal electron temperature surrounding with decreasing in time electron temperature $T_e(t)$ is considered in sections 4 "Second type break off" and 5 "Conductive decrease of pressure and appearance of tensile stress".

Problem concerning strength of two-temperature (2T) matter is considered in sections 6 "Two-temperature nucleation in stretched metal" and 7 "Two-temperature strength of gold". Finally comparing the strength versus values of negative pressures we conclude that spalling of extremely thin 7–10 nm spallation plate is possible.

2. Thermal fluxes

We consider ultrashort laser pulses with duration ~ 100 fs and absorbed fluencies 40–70 mJ/cm². Thickness of a skin in gold is ≈ 15 nm for optical wavelengths. During the pulse almost all absorbed energy accumulates in electrons inside a skin-layer. Indeed, power of electron-ion coupling is small to cool down electrons during a pulse. Conduction loses from a skin also are small at a time scale ~ 100 fs.

During a pulse an electron-ion coupling transits less than 1% of absorbed energy from electrons to ions. Electron heat conduction takes away 5–30% of absorbed energy.

The rate $\alpha(T_e - T_i)$ of electron-ion energy transfer is defined by the difference $T_e - T_i \approx T_e$ and by the coefficient of electron-ion coupling $\alpha \sim (0.5\text{–}2) \times 10^{17}$ W/K/m³ [27,28]. It was supposed that $\alpha \sim 0.22 \times 10^{17}$ W/K/m³ in the experimental paper [29], see abstract in this paper. The value $\alpha = 0.3 \times 10^{17}$ W/K/m³ was taken in the paper [24], see page 2, right column in this paper.

The cooling power of electrons per unit of volume due to coupling is $\approx \alpha T_e$. Electron temperature defined from electron internal energy in a skin is

$$T_e \sim \sqrt{2(F_{\text{abs}}/d_{\text{skin}})/\gamma} = 28[F_{\text{abs}}/(60 \text{ mJ/cm}^2)]^{1/2}[\gamma/(100 \text{ J/K}^2/\text{m}^3)]^{-1/2} \text{ kK}$$

for skin depth $d_{\text{skin}} = 15$ nm. Here F_{abs} is absorbed fluence. Energy transferred to ions during
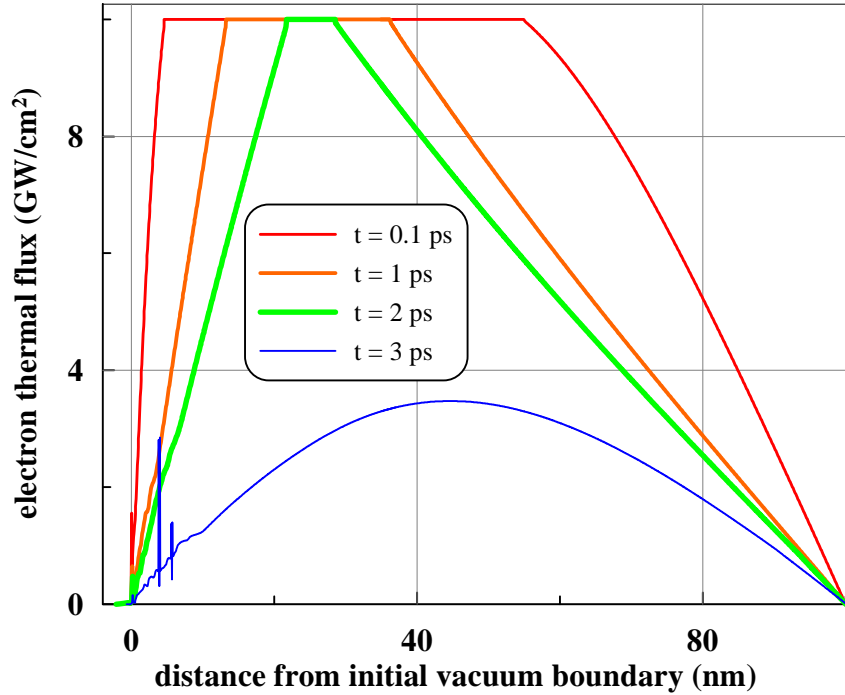
Figure 1. Simulation of the case $F_{abs} = 60$ mJ/cm^2, gold $d_f = 100$ nm, $\tau_L = 0.1$ ps, $q_l = 10$ GW/cm^2. Electron thermal flux drops down as a result of homogenization of T_e across a film thickness.

a laser pulse is

$$\alpha T_e \tau_L = 0.28[\alpha/(10^{17}\ \text{W/K/m}^3)][T_e/(28\ \text{kK})][\tau_L/(0.1\ \text{ps})]\ \text{GPa} \qquad (1)$$

here τ_L is duration of a pulse, GPa $= 10^9$ J/m^3. This is small amount (less than percent) relative to the internal energy

$$F_{abs}/d_{skin} = 40[F_{abs}/(60\ \text{mJ/cm}^2)][d_{skin}/(15\ \text{nm})]^{-1}\ \text{GPa} \qquad (2)$$

accumulated in electrons in a skin at the end of a pulse. Ion temperature increases on 110 K thanks to ion heating (1) if we assume that an ion heat capacity is given by Dulong–Petit law.

Increase of electron pressure at the end of a pulse is approximately equal to the value given by expression (2) because an electron Grüneisen parameter is $\Gamma \approx 1$ [30].

Radiation flux absorbed in a skin is

$$I_{abs} = 600[F_{abs}/(60\ \text{mJ/cm}^2)][\tau_L/(0.1\ \text{ps})]^{-1}\ \text{GW/cm}^2. \qquad (3)$$

Electron heat conduction flux from a skin is

$$q = \kappa \nabla T_e = 190[\kappa/(1000\ \text{W/K/m})][T_e/(28\ \text{kK})][d_{skin}/(15\ \text{nm})]^{-1}\ \text{GW/cm}^2. \qquad (4)$$

The one side total electron flux of energy inside gold is

$$q_{lim} = (1/2)\gamma T_e^2 v_F = 500[\gamma/(100\ \text{J/K}^2/\text{m}^3)][T_e/(10\ \text{kK})][v_F/(10^8\ \text{cm/s})]\ \text{GW/cm}^2, \qquad (5)$$

here v_F is Fermi velocity, expression $(1/2)\gamma T_e^2$ estimates density of internal electron energy E_e per unit of volume, see also appendix B. This is obvious absolute upper limit for thermal transport.
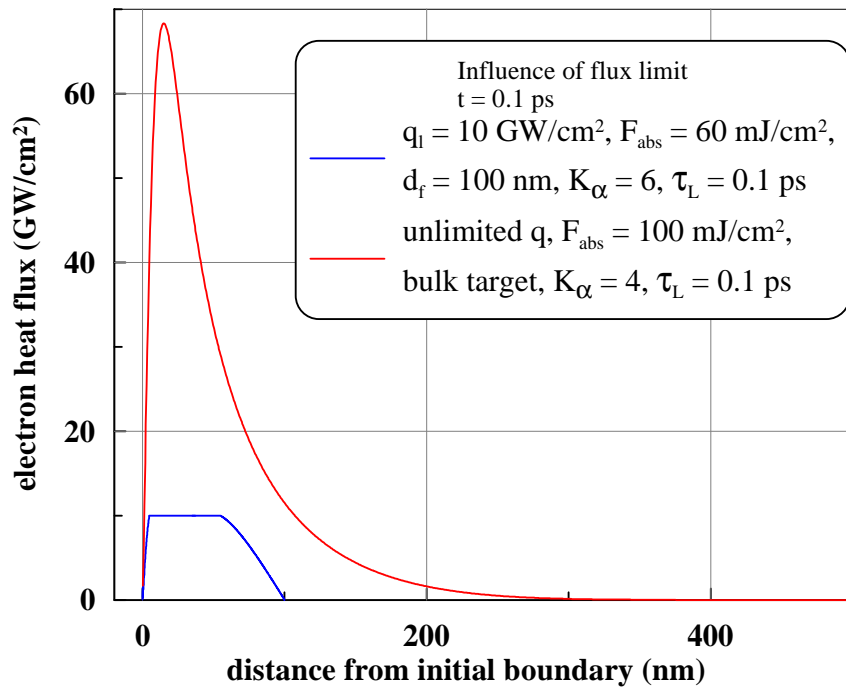
Figure 2. Comparison of the 2T-HD simulations with and without the flux limiter q_l. Coefficient K_α defines strength of amplification of electron-ion coupling parameter α (7 with increasing temperature T_e.)
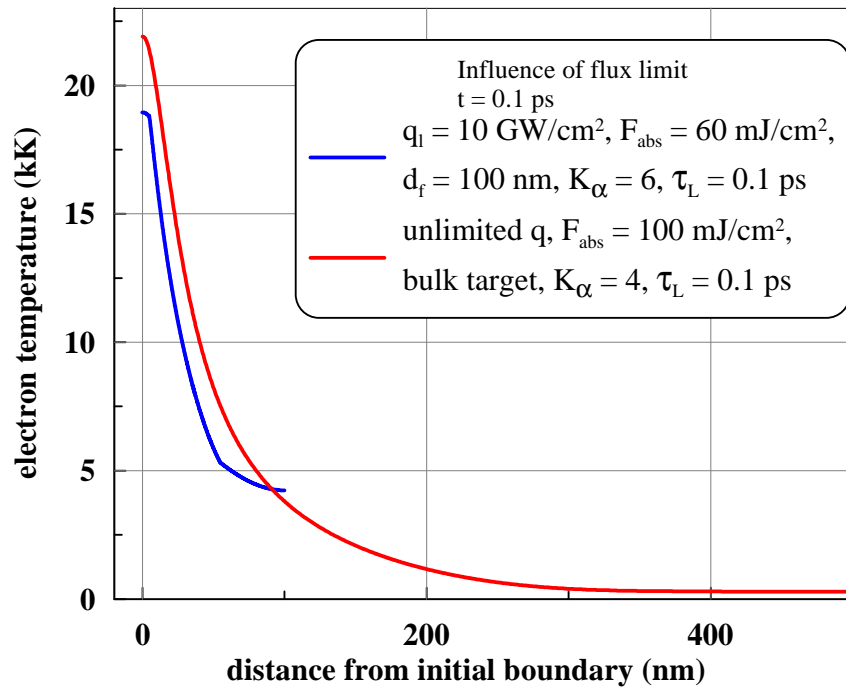
Figure 3. Comparison of the instant profiles of T_e from the 2T-HD simulations with and without the flux limiter q_l.
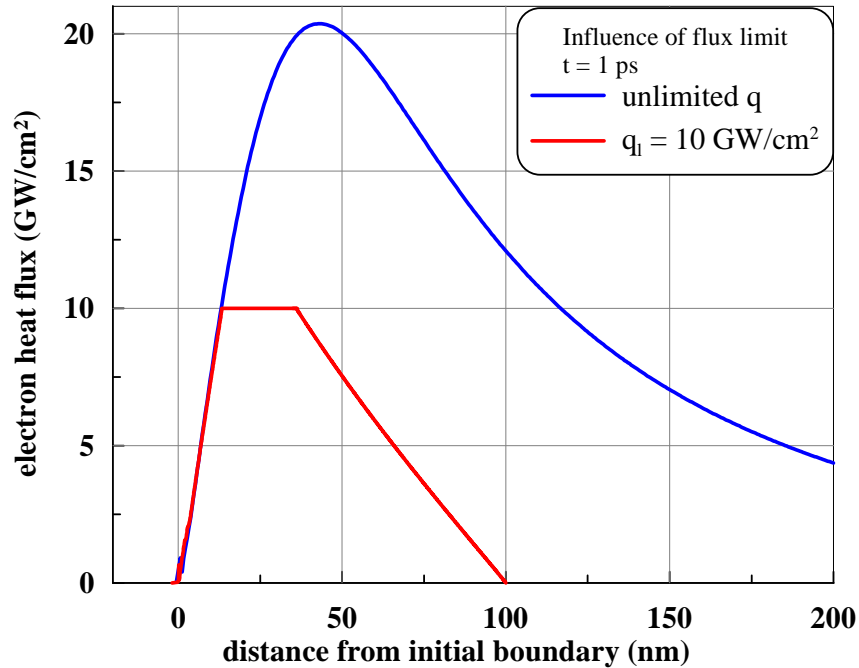
Figure 4. Comparison of the instant profiles of q. Parameters of the two runs are the same as it is written in figure 2. Flux q decreases with time because the differences of T_e across a target become smaller, see figure 5. In a thin film $d_f < d_T$ the decrease of differences of T_e proceeds faster (quick homogenization of T_e) than in a bulk target.

The electron flux q (4) quickly decreases because temperature T_e differences, inverse spatial scale for T_e, and a coefficient κ all decreases. Two-temperature simulations with the unlimited electron thermal flux show that there is a two order of magnitude drop of a flux $q = -\kappa \nabla T_e$ from a maximum value (3) in 2–3 ps for a 100 nm gold film. The decrease of the temperature T_e differences (homogenization of T_e) gives the main contribution to this drop in a thin film.

Expression (5) gives the absolute limit. Real saturation of electron energy transport should be achieved at smaller fluxes of the order of 1–10% from the value (5). Next section presents typical example of a 2T flow under this condition.

3. Two-temperature flow

We use a code integrating a set of 2T hydrodynamics (2T-HD) equations in Lagrangian variables (see, e.g., [30]) to simulate action of an ultrashort laser pulse onto 100 nm thick gold film. We limit electron flux at a 2% level of the value (5): above $q_l = 10$ GW/cm^2 the electron thermal flux q equals to q_l, while below this value the usual expression $q = -\kappa \nabla T_e$ is used. Corresponding profiles of thermal flux are shown in figure 1. The boundaries of a film thermally insulate the film: $\nabla T_e = 0$ at the boundaries. Therefore flux q has a zero values at the boundaries. Electron-ion coupling corresponds to $K_\alpha = 6$ (low rate of e-i exchange). Absorbed energy is $F_{\text{abs}} = 60$ mJ/cm^2.

The electron thermal flux decreases with time in figure 1, thus at $t \approx 2$ ps the limitation q_l finishes its limiting function. Below the limit q_l the maximum of the electron thermal flux q corresponds to the inflection point at the instant electron temperature profile $T_e(x, t = \text{fix})$.

Influence of the flux limiter q_l is demonstrated in figure 2. Indeed, at very early stage the cutting of an electron flux changes the flux significantly. But the instant distributions of electron temperatures T_e are not so much affected, see figure 3. Later the limited and unlimited flux

6
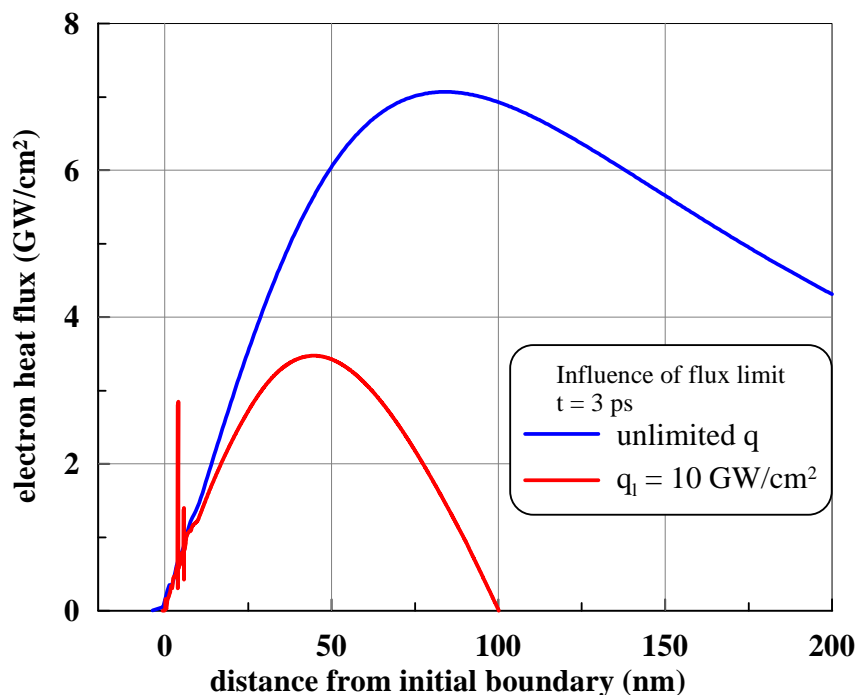
Figure 5. Comparison of the profiles of q for the instant $t = 3$ ps when the flux drops below the limit $q_l = 10$ GW/cm^2.

profiles $q(x, t = \text{fix})$ become closer to each other. This is shown in figures 4 and 5. After approximately 2 ps the flux q in the case of a thin film is smaller than the flux in the case with unlimited flux. This is so mainly because the electron temperature differences are smaller for a thin film relative to a bulk target. The perturbations of flux in few points in figure 5 (at the red curve corresponding to the flux limited simulation) appear as a result of beginning of nucleation in the hydrodynamic scheme which includes criterion of nucleation.

Comparisons of the electron temperature profiles are presented in figures 3, 6, and 7. The simulations with and without flux limitation are shown. In a thin film the electron temperature T_e distributions become close to homogeneous distribution across a whole film after the instant approximately 3 ps.

Hydrodynamics of sound propagation is important for analysis of spallation at an early stage. The rarefaction wave is created by an ultrashort laser action. Figure 8 shows the penetration of the rarefaction along an electron temperature profile which is spatially homogeneous for this wave but changes in time. At the stages shown in figure 8 these temporal changes are caused mainly by the heat conduction cooling of a surface layer. Let us mention that the hydrodynamic rarefaction very weakly affects electron temperature profile at the early stage when thermal conduction coefficient is high. We do not see any appreciable perturbation connected with the rarefaction wave on the T_e profile in figure 8. Thus we can say that dynamics of expansion of gold at an early stage proceeds in the T_e isothermal surroundings.

History of cooling of a surface is shown in figure 9. There are two dependencies for electron temperature for the case without flux limit (blue and green dashed curves). The blue curve gives instant temperature of a surface, while the green dashed curve corresponds to electron temperature T_e averaged along a skin depth 15 nm. These two curves are close to each other. This means that electron temperature is very homogeneous at the spatial scale of tens nanometers.
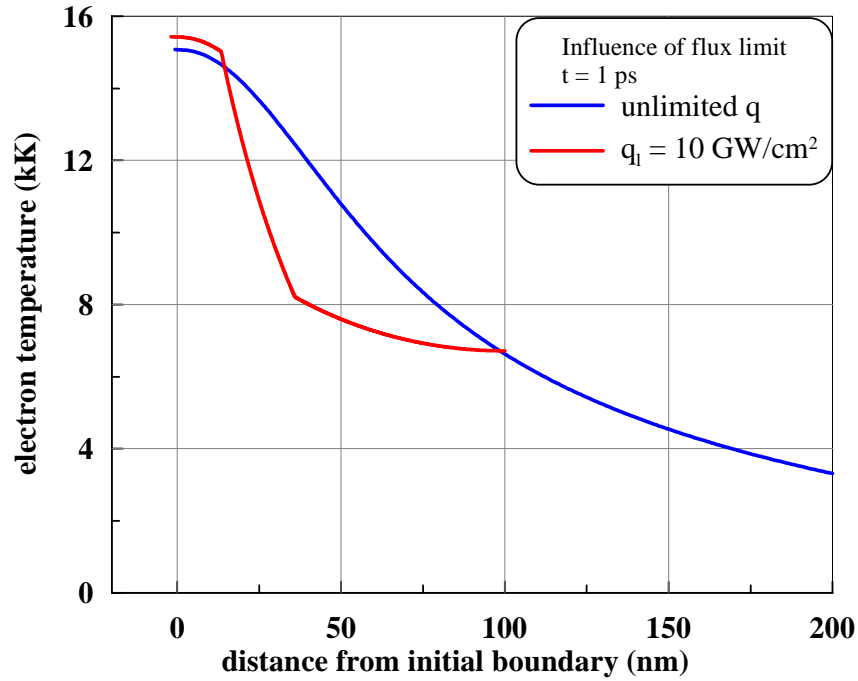
Figure 6. Instant electron temperature T_e distributions for limited and unlimited cases (corresponding parameters are listed in figure 2). At this instant a sound wave beginning its travelling from the vacuum boundary (when a pump arrives) passes 3 nm. We see that this wave travels inside the region where T_e is approximately constant value.

In the next section we use the time dependence $T_e(t)$ from figure 9 for a flux limited case to simplify the problem. We exclude energy equation for electrons from the set of the 2T equations. We use an approximate analytic expression

$$T_e(t) = 16.4(t_{ps} + 0.4)^{-1/3} \text{ kK} \qquad (6)$$

for the spatially homogeneous distribution of electron temperature instead of the electron energy equation; here t_{ps} is a time interval elapsed from the maximum of a pumping pulse. This $T_e(t)$ distribution should be homogeneous on the scale $c\,t$ of the order of 10 nm because we will consider propagation of a rarefaction wave during the first few picoseconds inside the surrounding with electron temperature variable with time, here $c \approx 3$ nm/ps is speed of sound in gold.

Electron-ion coupling parameter α and electron thermal conductivity κ used in our 2T-HD simulations are presented in figures 10 and 11.

Electron-ion coupling parameter is approximated by expression

$$\alpha(\rho, T_e) = \left(0.2 + \frac{4.3}{K_\alpha} \frac{T_{eV}^{3.6}}{1 + T_{eV}^{3.5} + 0.9 T_{eV}^{4.1}}\right) \left(\frac{\rho}{\rho_0}\right)^{5/3} \times 10^{17} \text{ W/K/m}^3. \qquad (7)$$

Here electron temperature T_{eV} is given in eV, K_α is a parameter defining the "height" of the function (7) in its high temperature part. The cases shown in figure 10 correspond to different values of K_α. At low temperatures T_e the function (7) begins from the experimentally confirmed value 0.2×10^{17} W/K/m^3 [31]. It is important that at small temperatures T_e our calculations [32] begin from the experimentally measured value [31] without any adjustment.

Electron thermal conductivity κ shown in figure 11 was studied in papers [28, 32–34]. Corresponding programs are presented in appendix A below.
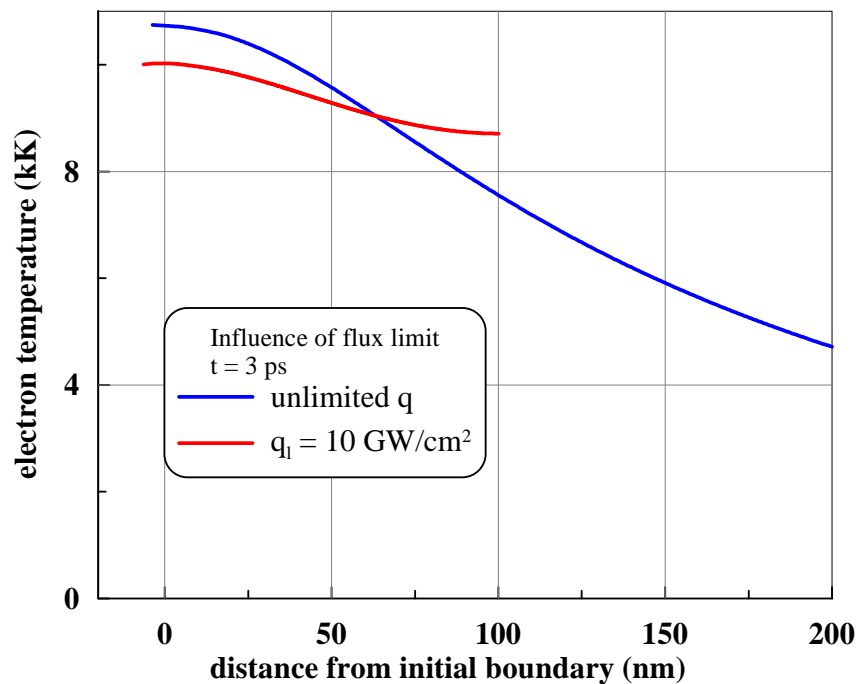
Figure 7. Comparison of the profiles of T_e for the instant $t = 3$ ps. Temperature T_e distribution becomes approximately homogeneous across a thin film.
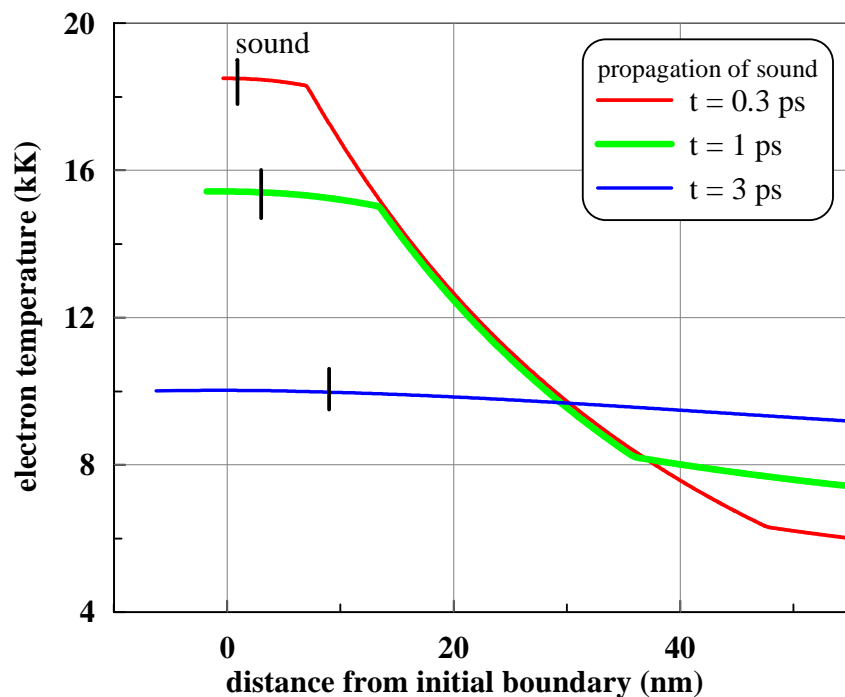
Figure 8. Propagation of a sound wave sent from a vacuum boundary into depth when the pump pulse has illuminated the boundary. We see that this wave propagates in a spatially homogeneous electron temperature T_e distributions, but temperature T_e decreases with time.
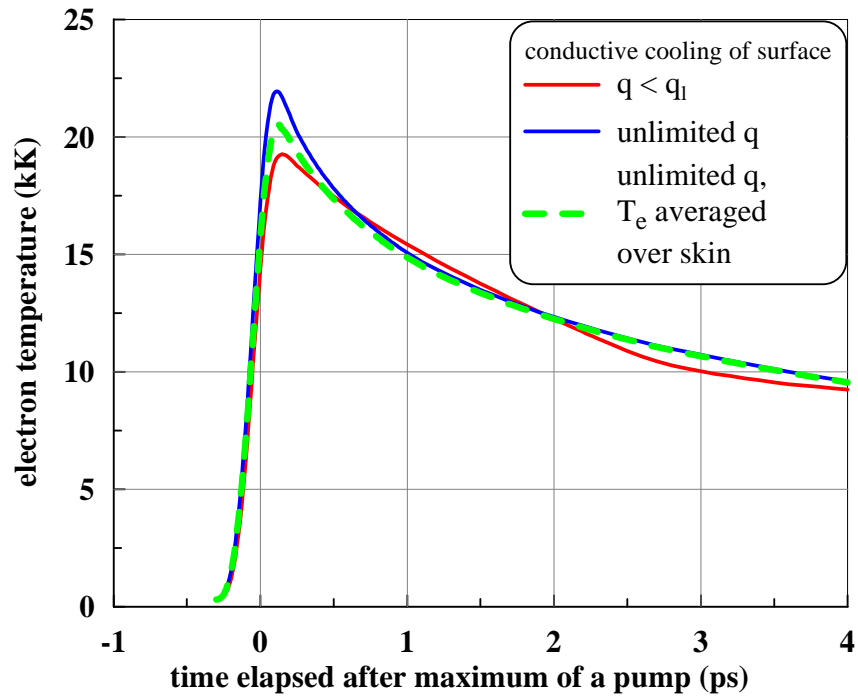
Figure 9. History of mainly conductive cooling of the vacuum surface: e-i coupling becomes important later. We compare the cases with and without limit for a thermal flux. Parameters of these two runs are given in figure 2.
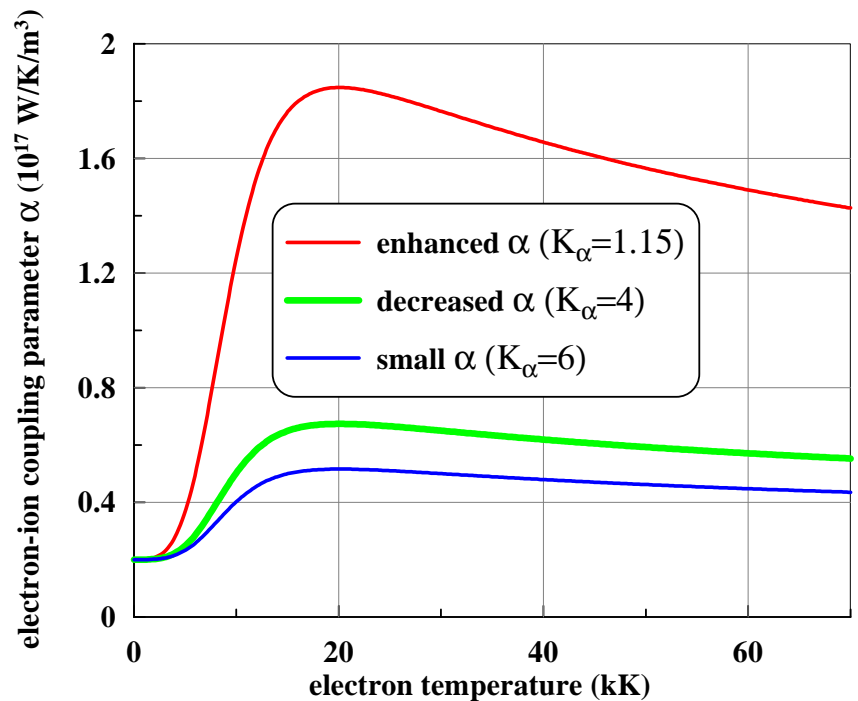
Figure 10. Electron-ion coupling parameter used in our 2T-HD simulations.

4. Second type break off

Spallation at the early stage is connected with rapid decrease in time of electron pressure p_e. At the same time, electron pressure p_e follows the electron temperature T_e distribution which
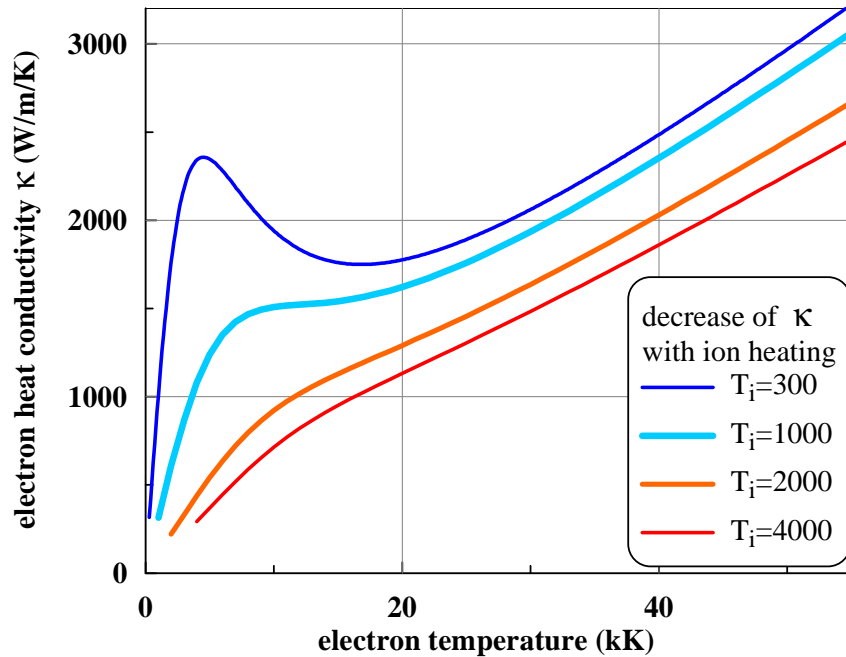
Figure 11. Electron thermal conductivity coefficient κ used in simulations. Calculation of this coefficient is presented in appendix A.2.

is very homogeneous. Therefore the p_e field is very homogeneous on a spatial scale ct covered by a rarefaction wave at the instant $t = 2$–3 ps; speed of sound is $c \approx 3$ nm/ps. The p_e field is spatially homogeneous not only in the part of a film undisturbed by rarefaction flow but also inside the rarefaction, see figure 17 below.

Heating of ions as a result of electron-ion energy transfer should be rather slow during these first 2–3 ps to have the early spallation. In this case electron pressure p_e dominates in the sum $p = p_e + p_i$ defining total pressure. Then electron pressure p_e dominates above ion pressure p_i ahead to the first characteristics of the rarefaction wave triggered by an ultrashort laser pump pulse. Thus expansion velocity follows electron pressure p_e decaying in time.

Total pressure governs dynamics of rarefaction. Difference between the value of total pressure ahead to the rarefaction covered layer from one side and vacuum pressure from the other side defines velocity of expansion in the case when total pressure ahead is permanent in time. Total pressure at the first characteristics decreases in time in our case. The rate of this decrease is rather slow; it is comparable with the rate of penetration of rarefaction wave. At this condition the approximate proportionality $\Delta p / z = u$ between the pressure difference and expansion velocity u remains; here z is an acoustic impedance. Then decrease of total pressure in time causes deceleration of expansion: velocity u decreases. The deceleration and appearance of negative pressure are tightly connected. It is clear that negative pressure of sufficiently large amplitude is necessary to induce spallation of condensed matter.

There are two main ingredients in our picture of the mechanism of the early type thermomechanical spallation. The first one is: the fast cooling of an electron subsystem thanks to a powerful electron thermal conduction transferring electron internal energy from the hot skin to the volume outside the skin. The skin volume is defined by thickness of a skin 15 nm. The outside volume is $(100 - 15)/15 = 6$ times larger. We see that electron energy from a skin in 2–3 ps is approximately homogeneously smeared along full thickness of our 100 nm film. Duration 2–3 ps of conductive cooling and smearing follows from simulation shown in figure 7.
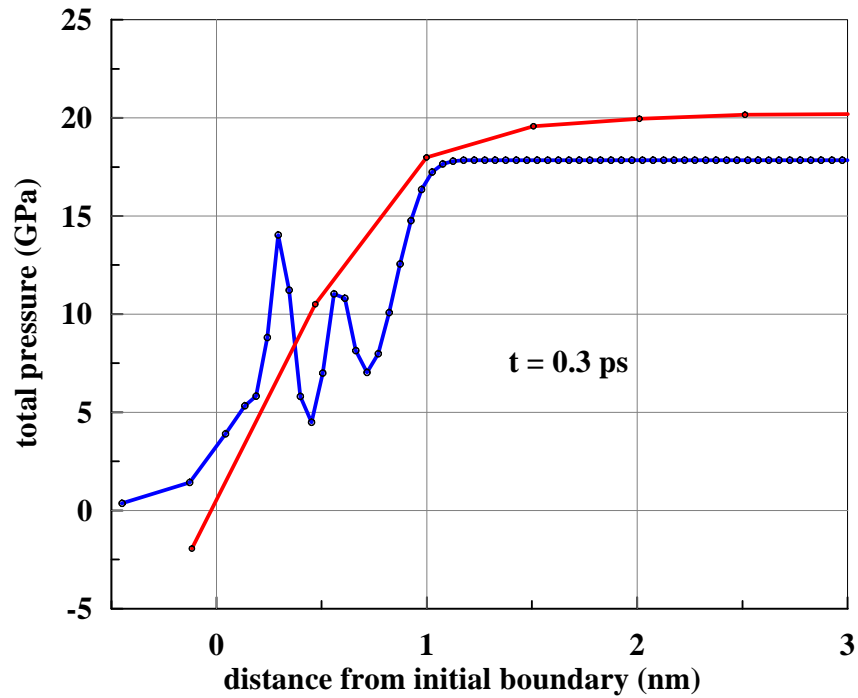
Figure 12. Total pressure instant profiles for the model with the spatially homogeneous $T_e(t)$ given by expression (6) and small rate of electron-ion energy exchange—we put the coefficient $\alpha = 0$ (7). The ionic part of equation of state was described differently for the blue and red curves, see text for explanations. The Lagrangian scheme of finite-difference integration has been employed. The Lagrangian steps are different for the blue (small step 0.05 nm) and the red (larger step 0.5 nm) curves. The points on the curves mark the instant positions of the Lagrangian steps. We see formation of the 2T rarefaction wave near the boundary of gold with vacuum.

Thus initial density of electron energy $E_e|_{ini}$ (per unit of volume) drops down to the 7 times lower value

$$E_e|_{smearing} = (d_f/d_{skin}) E_e|_{ini} = (100/15) E_e|_{ini}. \tag{8}$$

Corresponding decrease of electron temperature is $T_e|_{smearing} = T_e|_{ini}/\sqrt{5\text{--}7} = T_e|_{ini}/(2\text{--}2.5)$. Initial energy $E_e|_{ini}$ is accumulated solely in the skin electrons at the end of the pump pulse with subpicosecond duration; electron-ion cooling during a pump is negligible (1); conductive cooling during a pulse transfers out of a skin few tens percents of absorbed energy (4).

As was said above, electron pressure p_e [Pa=J/m^3] approximately equals to volume density of energy E_e [J/m^3]: $p_e \approx E_e$ because Grüneisen parameter for electrons is ≈ 1 [30]. Therefore cooling and smearing (8) induces a proportional drop of electron pressure in a skin:

$$p_e|_{smearing} = (d_f/d_{skin}) p_e|_{ini} = p_e|_{ini}/(5\text{--}7). \tag{9}$$

This is the main source of deceleration and generation of negative total pressures necessary for the second type break off.

Increasing absorbed energy F_{abs} we increase $p_e|_{ini}$ and the difference $p_e|_{ini} - p_e|_{smearing} = (0.8\text{--}0.9) p_e|_{ini}$. In this way we inevitably will achieve the second type ablation threshold.

Thickness $d_{spall-2} \approx c\, t_{min}$ of a spallation plate at the threshold for the second type spallation is defined not by a thickness of a skin layer d_{skin} but by the time interval t_{min} going to decrease total pressure to its minimum value.
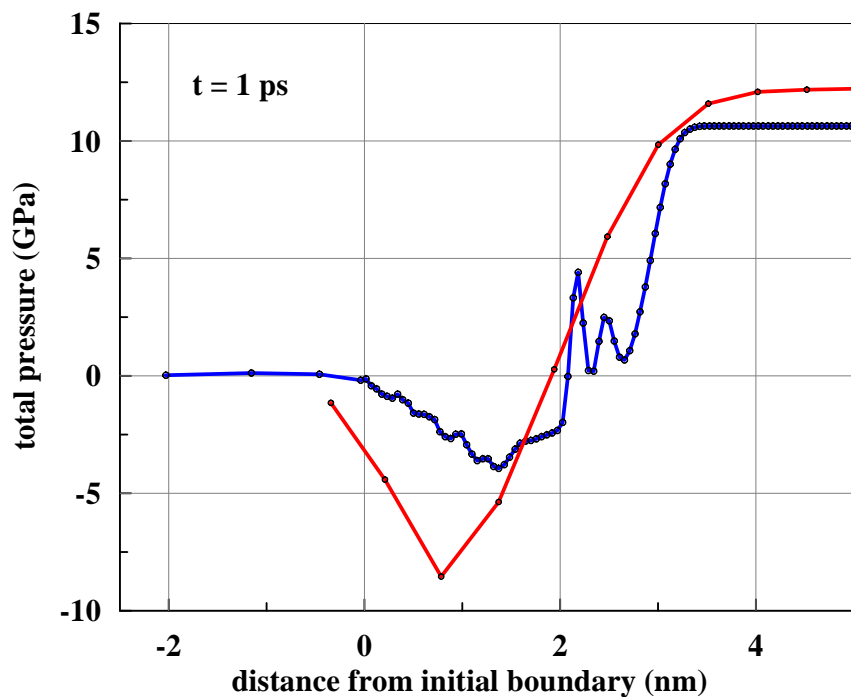
Figure 13. The beginning of formation of the negative "well" tensile in the *total* pressure profiles. Definitions of curves are given in figure 12.
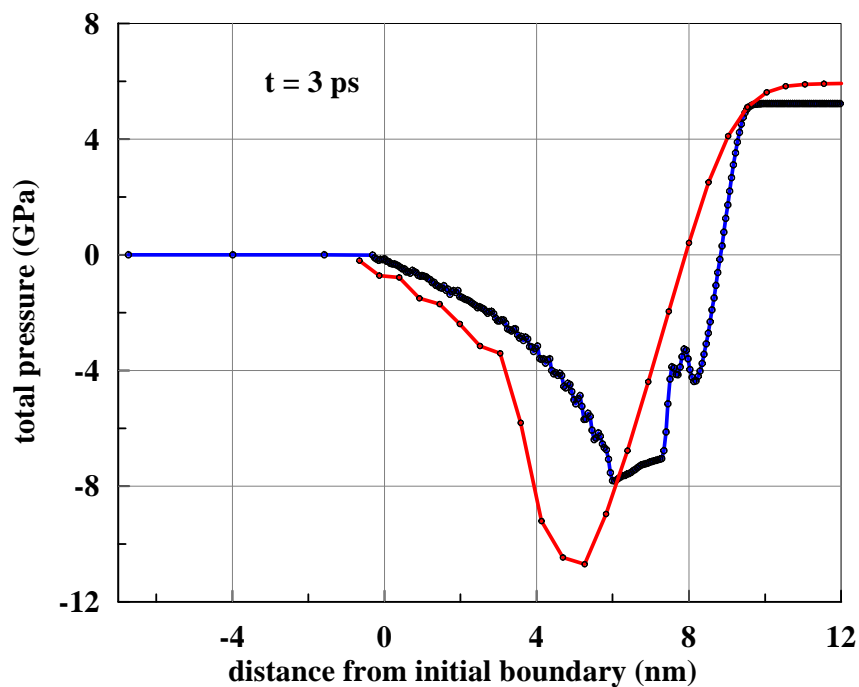
Figure 14. Gradual deepening of the negative well with time elapsing, compare with figure 13. We see also how the instant maximum of total pressure decreases with time. Definitions of curves are given in figure 12.
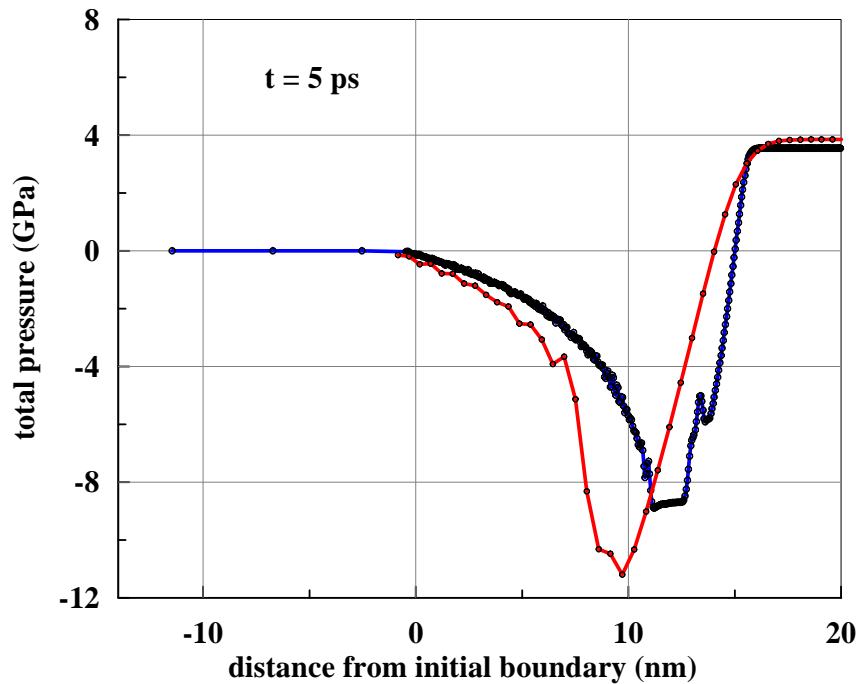
Figure 15. Deep negative well formed in few picosecond. Depth of the well is enough to induce break off of the spallation layer placed at the left side relative to the minimum of the well. Thickness of this spallation layer is 7–10 nm. Definitions of curves are given in figure 12.

The second ingredient of our picture of the second type ablation is linked to relatively slow heating of ion subsystem and slow increase of ion contribution to total pressure. In our picture conductive cooling leaves behind the electron-ion (e-i) exchange cooling. The redistribution of electron heat from skin to volume takes place during the first 2–3 ps. The e-i loses from electron subsystem is less significant at this time interval. But after that the conductive transport sharply drops down because electron temperature becomes approximately uniform across a film.

Now the e-i cooling of electrons transfer energy from electrons to ions. Almost all electron energy per unit of volume

$$F_{\mathrm{abs}}/d_f = 6[F_{\mathrm{abs}}/(60 \ \mathrm{mJ/cm}^2)][d_f/(100\mathrm{nm})]^{-1} \ \mathrm{GPa} \tag{10}$$

smeared along a whole volume of a film d_f transits into ion internal energy. It is said "almost" because at the final electron temperatures (~ 1–3 kK $\ll T_{\mathrm{F}}$) the electrons are highly degenerate, and their heat capacity is very low relative to the heat capacity given by the Dulong-Petit law; here T_{F} is Fermi temperature for gold.

Ion Grüneisen parameter $\Gamma_i \approx 3$ [12, 35] is approximately three times larger than electron Grüneisen parameter $\Gamma_e \approx 1$. Therefore total pressure inside the internal parts of a film begin to grow after the minimum of total pressure as electrons transfer their energy to ions; here we suppose that electron-ion temperature relaxation lasts shorter time than acoustic time scale d_f/c for dynamic relaxation of our 100 nm film. The maximum value of total pressure after the minimum is

$$\Gamma_i \, F_{\mathrm{abs}}/d_f = 18[F_{\mathrm{abs}}/(60 \ \mathrm{mJ/cm}^2)][d_f/(100\,\mathrm{nm})]^{-1} \ \mathrm{GPa}. \tag{11}$$

Estimate (11) follows from expression (10).

The history of total pressures p develops from
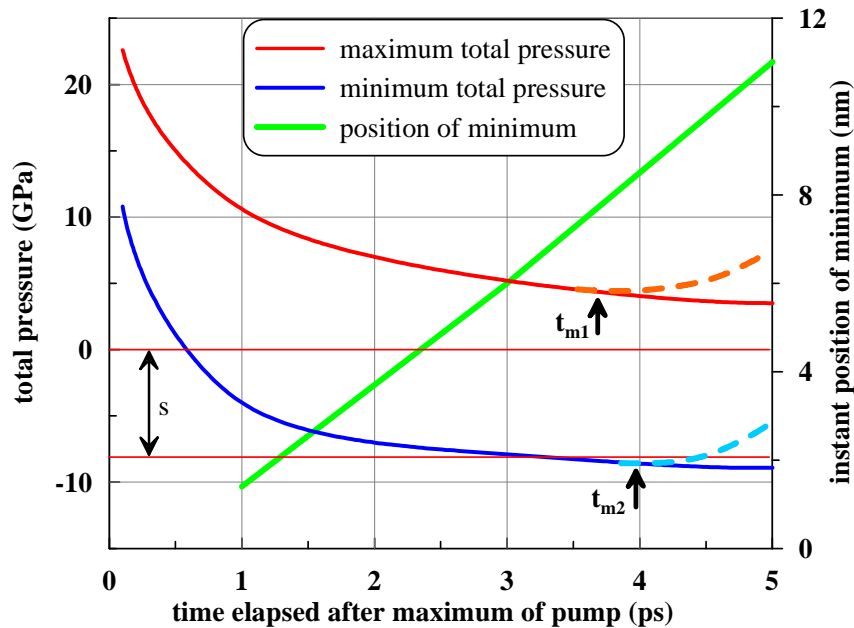
Figure 16. These plots generalize results shown in figures 12–15 above. One can see how the maximum of total pressure p (red curve) decreases as result of conductive cooling (6). The maximum is achieved ahead to the rarefaction front. The drop of p causes decrease of velocity and thus causes creation of tensile stress. The x-position in the laboratory frame and amplitude of p of the minimum are given by blue and green curves respectively. The minimum propagates with a local sound speed velocity. The arrow "s" marks the plausible strength of gold under 2T conditions. The dashed curves show results of e-i heating of ion subsystem which is more rigid (its Grüneisen parameter is larger) than electron subsystem. Thus total pressure begins to increase.

(i) the initial high value of mainly electron pressure $p \approx p_e|_{\max} \approx F_{\mathrm{abs}}/d_{\mathrm{skin}} \approx 40$ GPa for $F_{\mathrm{abs}} = 60$ mJ/cm^2 and $d_{\mathrm{skin}} = 15$ nm to

(ii) the minimum $p \approx 0.15\,p_e|_{\max} \approx 7$ GPa, and to

(iii) the maximum $\approx 0.5\,p_e|_{\max} \approx 18$ GPa (11).

Let us admit that the final maximum pressure (11) is enough to break off a film according to the first type thermomechanical ablation mechanism connected with the spatial inhomogeneity. Then near the first type threshold thickness of spallation plates will be approximately $d_f/2 \approx 50$ nm for $d_f = 100$ nm; this thickness is much thicker than thickness $c\,t_{\min} = 7$–10 nm in the case of the second type ablation.

Flight away velocity of the spallation plate is defined by an excess above threshold. It seems plausible that the threshold for the second type ablation is lower than the first type threshold. It seems also that at least near the thresholds the thick spallation plate from the first type break off flies slower than the thin plate from the second type break off.

5. Conductive decrease of pressure and appearance of tensile stress

Let us consider the electron conductive cooling, electron pressure drop, deceleration of a vacuum boundary, and creation of negative total pressure. As was said in section 4 we need small values of the electron-ion coupling parameter for this. We analyze the simplest model when electron temperature T_e is supposed homogeneous across a film and this temperature decreases in time as function $T_e(t)$ given by expression (6). This function describes conductive cooling in the vicinity
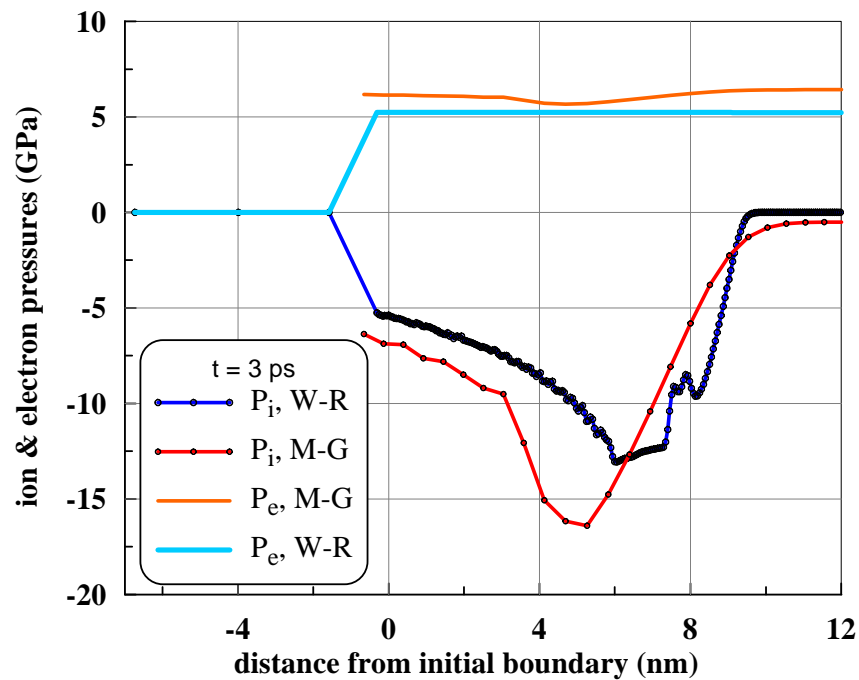
Figure 17. Electron p_e and ion p_i contributions to total pressure shown in figure 14. We see that p_i is small ahead the rarefaction front (because e-i heating is suppressed). But inside the rarefaction namely strong stretching of gold and decrease of p_i cause appearance of the well in the profile of total pressure shown in figure 14. Here W-R means wide-range equation of state, M-G is Mie–Grüneisen equation of state. Both are used to describe ion subsystem, see figure 12 with blue and red curves and text for explanations.

of the propagating rarefaction wave, see figure 8. We neglect also the electron-ion heating of ion subsystem. Therefore the thermal part (it is positive) of ion pressure is small. Only the negative part of ion pressure connected with strong expansion of matter in the electron pressure driven rarefaction wave is significant.

Figures 12–15 show development of the "well" with negative pressure in the profiles of total pressure. There are two curves in these figures. The blue one corresponds to the 2T-HD simulation with the wide-range equation of state of gold [20, 36–40] taken for an ion subsystem and addition of the electron equation of state from paper [30]. While the red curves present results obtained with the same electronic addition to the equation of state [30], but the ionic part has been constructed differently. Analytical Mie–Grüneisen equation of state has been used for an ion subsystem. The approach with Mie–Grüneisen equation of state gives more smooth profiles because the equation is analytical; while the wide-range equation of state is based on tables with interpolations inside the cells of the tables. Thus some fluctuation appears in the region where the table is sparse. But significant advantage of the wide-range tables against the Mie–Grüneisen approach is that the tables include description of melting. Nevertheless we see that the blue and red profiles are rather similar in spite of the difference in thermodynamic description and order of magnitude difference in the spatial step.

Figures 12–15 demonstrate the processes of formation and evolution of the non-steady non-self-similar rarefaction wave. This wave is not self-similar because total pressure p in the region ahead the rarefaction decreases with time. This is shown in figure 16 by the red curve. Deceleration of expansion and appearance of a layer with negative total pressures p is a result of cooling of a skin and drop of total pressure in the unloaded part ahead to the rarefaction front.
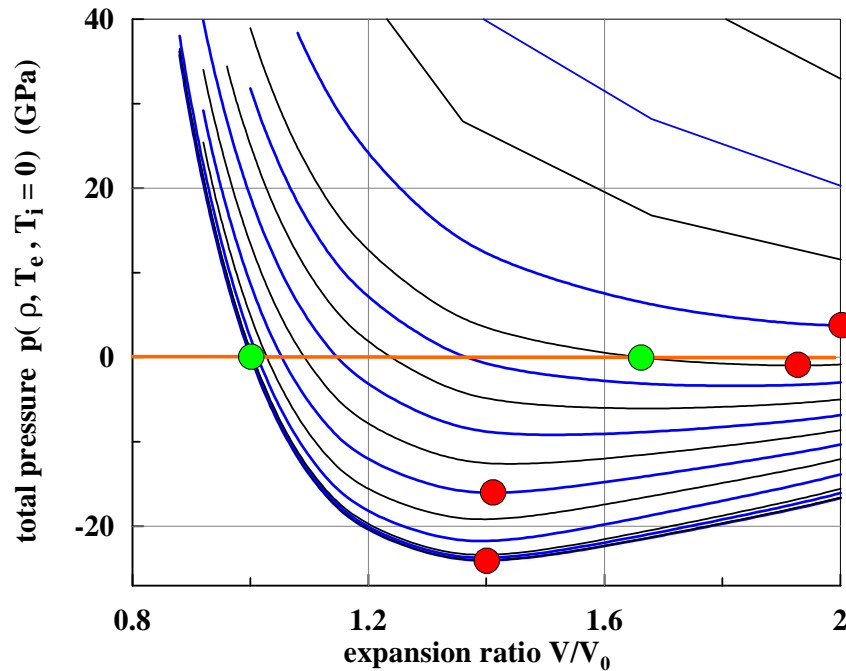
Figure 18. Isotherms $T_i = 0$, $T_e =$ const on the V/V_0–p plane are presented. They are obtained by the DFT VASP quantum calculations. Here p is total pressure, $V/V_0 = \rho_0/\rho$, $\rho_0 = 19.3$ g/cm^3. The set corresponds to electron temperatures $T_e = 1, 2, 3, 5, 7.5, 10, 12.5, 15, 17.5, 20, 22.5, 25, 30, 37.5, 45$, and 55 kK. The filled red circles mark minimums (spinodal) of total pressure for $T_e = 1, 12.5, 25$, and 30 kK. We see how strongly heating of electrons expands positions of minimums on specific volume over the familiar value $V/V_0 = 1.4$ at the cold curve $T_i = T_e = 0$. At the temperature $T_e = 26$ kK the minimum passes from negative $p < 0$ to the positive $p > 0$ region. The green filled circles give equilibrium volumes (binadal).

Total pressure p only decreases with time in the model with negligible electron-ion coupling α (7). This is shown in figure 16 by the red curve. In reality the decay of conductive cooling and transit to the electron-ion cooling of electrons will take place. When this change of the main cooling mechanism will take place depends on the value α (7). The change will induce increase of total pressure in the unloaded part as this was described in section 4.

Therefore the red curve in figure 16 will have a minimum point t_{m1}. This minimum point separates the regime with mainly conductive cooling from the regime with mainly electron-ion cooling shown in figure 16 by the dashed curve increasing p in time after the instant t_{m1}. As was said, when the instant t_{m1} corresponding to the minimum point on the red curve comes depends on α—it comes earlier for larger values α. The minimum t_{m2} of the blue curve is connected to the minimum t_{m2}. Thus increase of total pressure in the vicinity ahead to a rarefaction front will cause increase of total pressure in the minimum of the well—the well becomes less and less deep with time.

Rarefaction wave presented in figures 12–15 was obtained for suppressed electron-ion exchange condition. Ion temperature T_i was set equal to 300 K. This temperature is kept in time in the central region unaffected by rarefaction motion. Inside the rarefaction the temperature T_i decreases because an ion subsystem is adiabatically stretched–there is no heating source in the ion thermal equation.
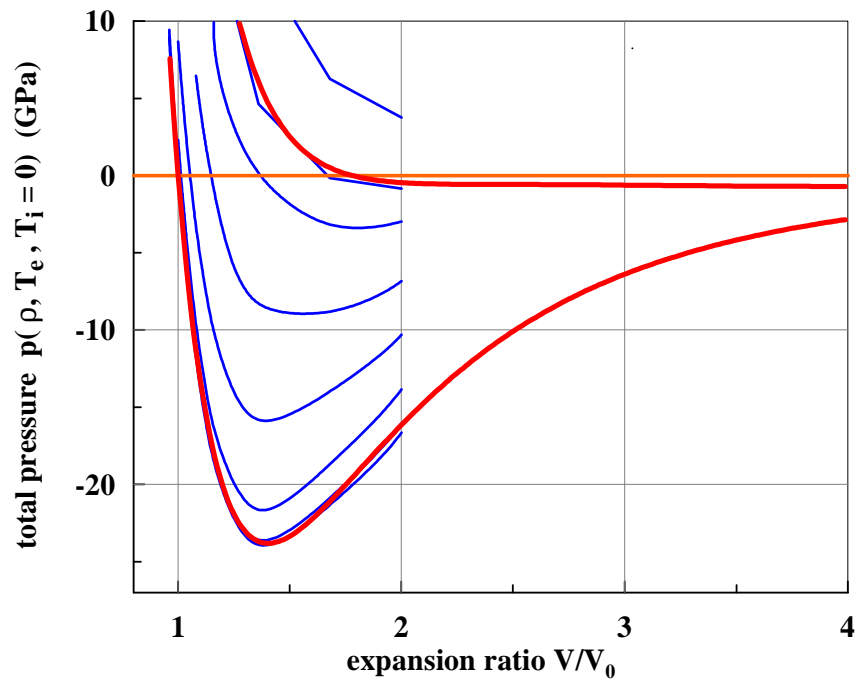
Figure 19. Comparison of DFT data with the approximation (13) for electron temperatures $T_e = 0$ (cold curve) and $T_e = 25$ kK (near the end of cohesive bonding). We continue the approximation up to a strong expansion degree.
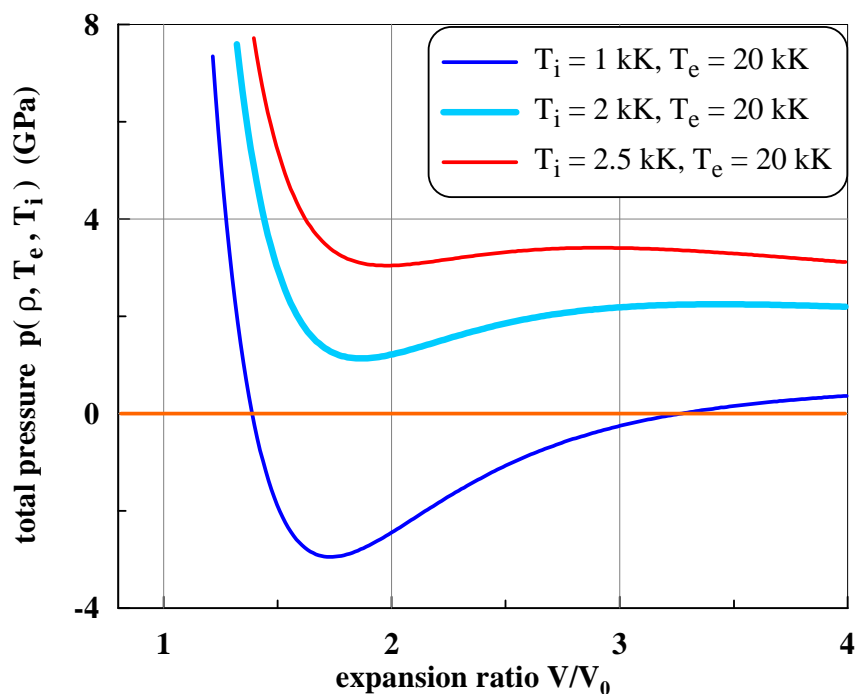
Figure 20. The isotherms for finite electron and ion temperatures are shown. They are calculated thanks to approximation (13).
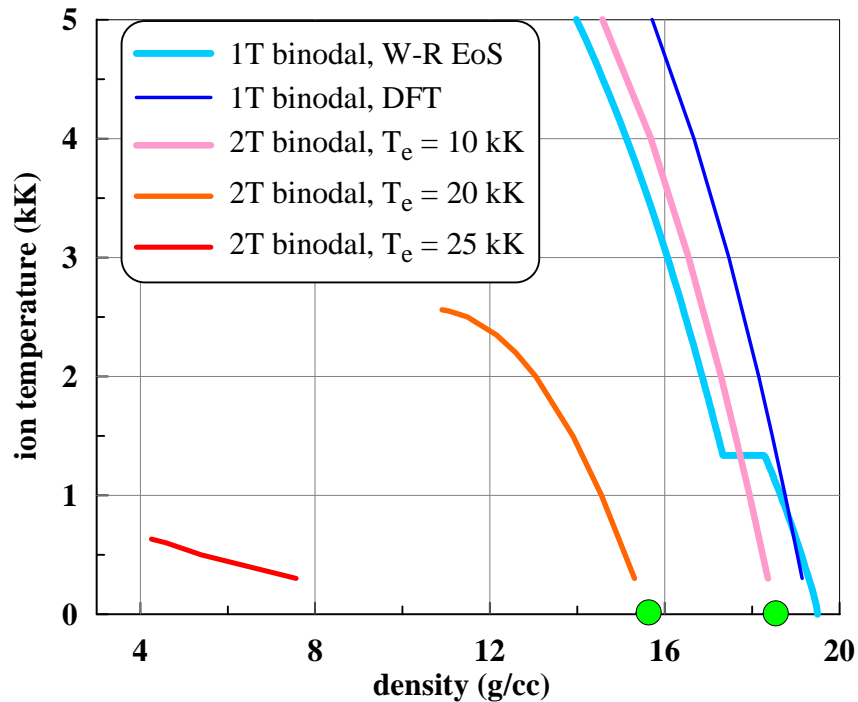
Figure 21. Projections onto the phase plane (ρ, T_i) of the cross sections made by the planes $T_e = $ const intersecting the 3D surface of binodal. The curves of cross-sections are obtained from equation (13), see text. W-R means wide-range equation of state. Two phase mixture of condensed and vapor phases locate below the surface of binodal.

6. Two-temperature nucleation in stretched metal

Figure 17 presents instant distributions of ion p_i and electron p_e pressures. Popular approach divides ion and electron pressures, says that ion pressure weakly depends on electron temperature $p_i \approx p_i(\rho, T_i)$, and imposes condition on nucleation on the ion pressure. Thus it is supposed that the work needed to create a bubble is $w = (16\pi/3)\sigma^3/p_i^2$, and the probability to nucleate a bubble is $\propto \exp(-w/k_B T_i)$, where σ is surface tension. We have to use ion temperature for calculation of the probability.

Here we develop another view. Electron pressure does not act inside an empty bubble or inside a bubble with vapor content. Therefore the total pressure (not p_i) drives expansion of nucleus:

$$w = (16\pi/3)\sigma^3/p^2. \tag{12}$$

Total pressure $|p|$ in the minimum of the well is smaller than $|p_i|$ because electron pressure is always positive, compare figures 14 and 17. Thus the work (12) with $|p|$ becomes significantly larger than the same work with $|p_i|$.

This condition strongly stabilize two-temperature liquid against nucleation allowing longer existence of a metastable phase and much higher stretching of matter relative to the one-temperature case. Thus the way to production of highly excited and strongly expanded condensed matter is open. It is plausible that the expanded gold remains in metallic state. These excited and expanded states may be probed in the pump-probe experiments, see, e.g., [7, 29, 41–47].
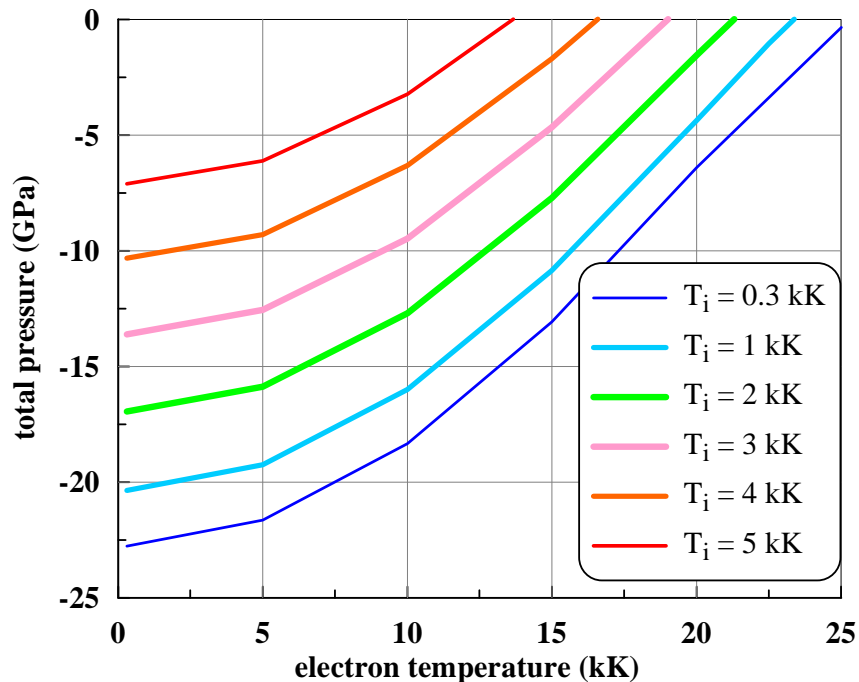
Figure 22. 2T spinodal $p_{\mathrm{sp}}(T_e, T_i)$ of gold.

7. Two-temperature strength of gold

We run a set of the quantum-mechanical DFT (density functional theory) VASP [48] simulations in local density approximation to define 2T equation of state of gold; see papers [39, 49–51] devoted to the similar problems. Results of simulations are presented in figure 18. These runs correspond to the FCC lattice of gold with ions fixed in their equilibrium positions because $T_i = 0$. The green and red filled circles in figure 18 corresponds to the projection of the binodal surface onto the $T_i = 0$ plane in the three-dimensional space of parameters (ρ, T_i, T_e) of the 2T equation of state.

Let us approximate the isotherms shown in figures 18 and 19. The approximation is

$$p = \rho_0 \, c^2 \, (1 - X)/[1 - 0.62(1 - X)]^5 + 25 \exp(-X)T_e^2 + 0.00732 T_i/X \text{ GPa.} \qquad (13)$$

In equation (13) value p is total pressure, c is sound speed, $X = V/V_0$, T_e is in [eV], while T_i is in [K]. There are three terms in equation (13). The first one is a corrected prolongation of a shock Hugoniot adiabatic curve into negative region $p < 0$. It gives us cold pressure depending only on density. The second and the third terms correspond to the Mie–Grüneisen approach, but separately for electron and ion internal energies. The second terms has been adjusted to results of the DFT modeling. The third term presents contribution of ionic thermal energy. It equals to $\Gamma_i E_i = \Gamma_i 3k_B T_i$, where k_B is Boltzmann constant. We take $\Gamma_i = 3$ for gold (see figure 3 in [12] and [35]) and neglect dependence of Γ_i on density ρ.

Combined influence of electron and ion heating is shown in figure 20. Let us mark that the isotherms with the minimum in the range $p > 0$ seems are possible at enhanced heating.

Three dimensional binodal surface of the 2T equation of state is analyzed in figure 21. The blue curve named "1T binodal (W-R)" gives the curve of sublimation, triple point, and the boiling curve according to the wide-range equation of state [36, 37].

If we put $T_i = 0$ and vary electron temperature then we come to the set of the isotherms shown in figure 18. Below the limit $T_e \approx 26$ kK ≈ 2.2 eV the left branches of the isotherms in

figure 18 have intersection with the zero level of total pressure $p = 0$. These intersections are marked by the green filled circles in figure 18. Increase of electron temperature T_e increases electron pressure p_e. This pressure expands gold. Thus density of the equilibrium state drops and the green circle on the axis $V \propto 1/\rho$ in figure 18 moves to the right side.

The same green circles are shown in figure 21. They move in the direction of decrease of density as electron temperature T_e rises. As we increase temperature T_e, the green circles in figure 21 shifts to the left side along the axis $T_i = 0$, and the area under binodal becomes smaller and smaller. Finally at temperature $T_e \approx 26$ kK ≈ 2.2 eV the binodal disappears. It is interesting to follow this process in figures 18 and 21 simultaneously.

We use equation (13) to plot 2T binodals in figures 18 and 21. We fix temperatures T_e and T_i and find root $\rho = \rho(T_e, T_i)$ of equation $p(\rho, T_e, T_i) = 0$ (13). This root gives us the 3D binodal surface over the plane (T_i, T_e).

In the 1T case $T_e = T_i = T$ the root $\rho = \rho(T, T)$ of equation $p(\rho, T, T) = 0$ (13) gives us the 1T binodal shown in figure 21 (deep blue curve). It goes close to the wide-range 1T binodal (blue curve with a step of the triple point). But DFT of crystal used in our DFT runs does not allow considering the case of fluid. Thus our DFT binodal does not have a step.

The ultimate strength of gold is defined by pressure at the 2T spinodal. We use equation (13) to obtain spinodal $p_{\rm sp}(T_e, T_i)$. Derivative dp/dV of expression (13) has been calculated. We fix temperatures T_e, T_i and find root $\rho_{\rm sp}(T_e, T_i)$ of equation $dp/dV = 0$. After that we calculate pressure at the spinodal surface

$$p_{\rm sp}(\rho_{\rm sp}(T_e, T_i), T_e, T_i).$$

The results are shown in figure 22.

Tensile pressures achieved in simulations shown in figures 12-15 are near the spinodal presented in figure 22 for typical temperatures $T_e = 10$–15 kK, $T_i = 1$–3 kK. Thus ablation of a thin spallation plate through the second break off mechanism is possible. As a result the spallation plate 7–10 nm thick appears.

The maximum of a tensile stress in our 2T hydrodynamics simulations is achieved at the instants $t_* = 2$–3 ps at the depth $c\,t_* \approx 7$–10 nm. This maximum triggers nucleation or acoustic instability. This depth defines thickness of a spallation plate. Similar thicknesses were obtained in paper [24]. We can not compare the instants when maximum tensile stress is achieved in [24] with our results because the profiles of total pressures at the first picoseconds are not given in [24]. Visible gap between the spallation plate and the rest of a target appears between 10 and 20 ps, see figure 2(a) in [24]. This time interval is significantly delayed relative to our nucleation instants t_*. This may be explained by slow expansion of the banks of the developing gap.

8. Conclusion

We analyze above the new aspects of thermomechanical ablation by an ultrashort laser pulse. The most important problem solved in paper concerns the early stage of ablation. Usually people consider thermomechanical ablation caused by deceleration related to spatial inhomogeneity. This is inhomogeneity or of a heat affected zone d_T in a bulk target, or thickness of a film d_f in case of a thin film when $d_f < d_T$. The scale d_T is ~ 100–200 nm for gold.

In our paper the alternative case is studied. In this case not a spatial inhomogeneity is a reason of deceleration, appearance of tensile stress, and nucleation. The reason is the fast decrease of total pressure at the first 2–3 ps (section 4).

We link the decrease of total pressure in time with fast conductive cooling of a skin layer strongly heated by absorption of a laser pulse. The decrease of total pressure (as a result of cooling of electrons at relatively more slow heating of ions) lasts during very short time interval 2–3 ps. After that total pressure begins to grow during the next finite time interval due to ion heating. It should be explained that we speak here about total pressure in a region close to the head of the propagating rarefaction wave but outside rarefaction flow.

In this connection we have studied thermal problem at the early stage. Electron heat fluxes are estimated (sections 2 and 3). It is significant (for conductive cooling of a skin) how thick is a thin film $d_f < d_T$ relative to thickness of a skin layer ($d_{\mathrm{skin}} \approx 15$ nm for optical lasers and gold). Indeed, the rest of a film (which remains cold during the subsecond laser pulse) serves as a cooling capacity taking heat from a skin. If a film is $d_f \sim d_{\mathrm{skin}}$ then the fast cooling (thanks to quick transfer of a heat into capacity) is absent. Thus the alternative mechanism of break off becomes impossible.

In the alternative case, thickness of spallation plate is small. It is equal to 7–10 nm. While in the case of usual thermomechanical ablation, at the threshold, it is approximately a half of thickness of a film. It is 40–50 nm for our film 100 nm thick.

We develop the models for 2T equation of state, thermal conductivity, and electron-ion coupling. From equation of state the spinodal and strength of the 2T system is calculated (section 7).

We calculate expansion at the early stage and find that negative pressures appearing thanks to fast cooling have enough amplitude (section 5) to break off thin (7–10 nm) spallation layer (section 5).

Acknowledgments

Appendix A. Calculation of two-temperature electron thermal conductivity

Here we present two programs developed for calculation of coefficient of 2T heat conduction. They use the package of symbolic computations "Wolfram Mathematica". Figure 11 is obtained using the second program. The first program gives slightly smaller values of coefficient κ. This is the programs for gold (Au). The program for calculation of coefficient κ for aluminum was developed in [52].

Appendix A.1. The first program "2T conduction"

```
(*Electron heat conductivity of gold*)

(*Approximations:

1. Two-parabolical DoS (electron density of states) with energies
 and electron numbers

 as functions of Te and V

2. Drude-approximation for the frequency of electron-ion collision:

nu_ei=e^2*n_s*rho_e/m_s, here n_s, m_s - concentration of s-electrons,

mass of one s-electron, rho_e - electrical resistivity

3. rho_e at T~Tmelting - fitting of experimental data, rho_e at T>>T_melting -

Mott's limit, rho_e as function of volume - rho_e (V)~V^(2G-1/3),

G - Gruneisen parameter
```

4. We use rho_e (V)~V^(2G-1/3) for solid AND liquid gold,
 although in the latter case it may be wrong*)

(*Part I *)
(*Parameters of two-parabolical model*)

Z=11; (*total number of valence electrons*)

nat=6.022*19.28/196.97; (*atomic concentration*)

na=nat*0.148*0.1; (*atom. concentr. in a.u.*)

a1v[v_]=8.370116055555545 +0.7592750000000095*v;
(* v = V/Vo *)

b1v[v_]=-0.07772823222222186+0.14376283333333298*v;

c1v[v_]=0.002928826666666666;

f[te_,v_]=a1v[v]+b1v[v]*(te/11605)+c1v[v]*(te/11605)^2;

zd[te_,v_]=f[te,v];

(* d-electron number as a function of volume and electron temperature*)

zs[te_,v_]=Z-f[te,v];

(* s-electron number as a function of volume and electron temperature*)

e1a[v_]=5.561611190476584 +1.088018939393126*v-4.577624458874042*v^2;

e1b[v_]=-0.1255257317697-0.068264699156441
*Sin[30.86751811350718*v-23.774835712];

e1c[v_]=41.134008963928 -126.487749601735 v+129.28817149158718 v^2
-43.947589435989 v^3;

e1[te_,v_]=e1a[v]+e1b[v]*(te/11605)+e1c[v]*(te/11605)^2;

e2a[v_]=25.177545055555527 -17.103274999999968*v;

e2b[v_]=3.3169602455555496 -3.7120671666666607*v;

e2c[v_]=-1.964970711111108+1.955094999999997*v;

e2d[v_]=0.2921434513388884 -0.29283181916666623*v;

e2[te_,v_]=e2a[v]+e2b[v]*(te/11605)+e2c[v]*(te/11605)^2+e2d[v]*(te/11605)^3;

```
es[v_]=5.8-5.15*v;
eF[v_]=24.8-16*v;

ES[v_]=eF[v]-es[v]; (*s-electron minimum energy as a function of volume*);

E1[te_,v_]=ES[v]+(es[v]-e1[te,v]);
```

(*d-electron minimum energy as a function of volume
 and electron temperature*);

```
E2[te_,v_]=ES[v]+(es[v]-e2[te,v]);
```

(*d-electron maximum energy as a function of volume
 and electron temperature*);

```
ms[te_,v_]=27.211*(3*Pi*Pi*na*zs[te,v])^(2/3)/(2*ES[v]) ;
```

  (*effective mass of s-electron*) ;

```
md[te_,v_]=27.211*(3*Pi*Pi*na*zd[te,v])^(2/3)/(2*(E1[te,v]-E2[te,v]))
```

(*effective mass of d-electron*)

(*Part II *)
(*Fittings of experimental data for electrical resistivity of gold*)

(*Experimental data used here was obtained by R.A. Matula

 (J. Chem.Ref. Data, V. 8, P .1147, 1979, doi:10.1063/1.555614*)

```
rhoesol[ti_]=0.000068837*ti+2.3187200000000002*10^(-8)*ti^2
```

 (*electrical conductivity of solid gold as function of temperature
 (ion temperature)*)

```
rhoeliq[ti_]=0.308244+0.000157144'*(ti-1337)
```

(*electical conductivity of liquid gold - this is approximation at temperatures

slightly above melting temperature at zero pressure*)

```
rholowT[ti_,v_]=If[ti<Tm[v],rhoesol[ti],rhoeliq[ti]] (*general formula*)
```

```
Grun[v_]=2.95*v^1.229 (*Gruneisen as function of volume*)
```

```
rlowT[v_,ti_]=rholowT[ti,v]*v^(2*Grun[v]-1/3)*(zs[1000,1]/zs[1000,v])^(2/3)
```

(*electrical conductivity at T <<T_Fermi as function of volume

and (ion) temperature*)

```
rMott=0.8
rhighT[v_]=rMott*v^(1/3)*(zs[55000,1]/zs[55000,v])^(2/3)
```

 (*Mott limit dependence from volume*)

```
rTi[v_,ti_]=((rlowT[v,ti])^(-4)+(rhighT[v])^(-4))^(-0.25)
```

 (*mathching of both fittings for electrical resistivity*)


```
(*Part III*)
(*Frequency of Drude collisions by Drude formula*)
```

```
(*constants and table data*)
hbar=1.054*10^(-27);
```

```
z2=(4.807*10^(-10))^2;
```

```
natsq3=(6.022*19.28*10^23/196.97)^(1/3);
```

```
L=4;
```

```
zz=zs[55000,1]
```

```
const=(3*Pi^2*L/zz^2)^(1/3)
```

```
rmaxCGSE=hbar/z2/natsq3*const
```

```
rmaxSI=0.2*rmaxCGSE*9*10^9*10^6*z2*natsq3^3
*rmaxCGSE/ms[1000,1]/(9.11*10^(-27))
```

```
nu0=6.425119880161749*10^14
```

```
constnu=nu0/rmaxSI
(*effective frequency of electron-ion collisions in accordance
 with Drude formula*)
```

```
 nuei[v_,ti_,te_]=
z2*natsq3^3*(1/v)*zs[te,v]*rTi[v,ti]*10^(-6)/ms[te,v]/(9.11*10^(-28)*9*10^9)
```


```
(*Part IV*)
(*gold two-temperature thermodynamics*)
```

```
(*volume and electron temperature dependent DoS*)
gs[e_,te_,v_]=1.5*zs[te,v]/v/(Abs[ES[v]])^(3./2.)*Sqrt[e+Abs[ES[v]]];
```

```
(*mean square of electron velocity*)
```

```
vs2[v_,te_]=
(2*Abs[ES[v]]+3*(te/11605))/ms[te,v]*(1.6022*10^(-19)/(0.911*10^(-30)));
```

```
(*fitting for electron chemical potential as function of electron temperature,
 the dependence from volume are omitted*)
```

```
mu[te_]=
27.211*5*10^(-10)*te^2/(1+4*10^(-9)*te^2)-5*10^(-10)*te^2*Exp[-te/11000];
```

```
(*electron internal energy*)
uvs[te_,v_]=
NIntegrate[gs[e,te,v]*e/(1+Exp[(e-mu[te])*11605/te]) ,

{e,-Abs[ES[v]],50}]*(nat*1.6022*10^(-19)*10^29)
```

```
 (*10^6 (CGSe to SI)/10^5( J/m^3/K)*)
```

```
(*electron specific heat*)
cvs[te_,v_]=D[uvs[te,v],te]/116050
```

```
(*gives a number of the electrons with energies below Fermi energy*)
NIntegrate[gs[e,1000,1],{e,-Abs[ES[1]],0}]
```

```
(*simple fit for electron specific heat*)
Cvss[v_,te_]=rc1[v]*te+rc2[v]*te^2+rc3[v]*te^3
```

```
(*Part V*)
(*construction of final expression*)
```

```
(*thermal resistivity due to electron-ion collisions*)
Sei[te_,ti_,vv_]=3*10^4*nuei[vv,ti,te]/((Cvss[vv,te]*10^5)*vs2[vv,te])
```

```
(*melting curve due to Lindemann law*)
Tm[v_]=1337*v^(2/3)*Exp[5.9/1.229*(1-v^(1.229))]
```

```
(*electron-electron contribution in heat conductivity
 at equilibrium density*)
kee1[te_]=0.041*te+2.5*10^9/te^1.5
```

```
(*volume factor multiplied on previous expression; x = V/Vo *)
volkee[x_]=If[x>1,x^1.4,If[x<1,x^2.4,1]]
```

```
(*electron-electron contribution as a function
 of electron temperature and density*)
kee[te_,x_]=kee1[te]*volkee[x]
```

```
(*parts of new formula of electron-phonon contribution
 in electron heat conductivity of solid gold*)
```

```
(*the fittings introduced hereafter were obtained using Sei *)
P1[x_]=19800*x^1.77
Q1[x_]=4
L1[x_]=3.6*x^2.95
M1[x_]=3500*(1+1/(1+12*(x-1)^2))
N1[x_]=40000/x-28500
B1[te_,x_]=L1[x]/(1+((te-M1[x])/N1[x])^2)+Q1[x]*Tanh[te/P1[x]]
alpha[x_]=0.82*x^5.3

(*electron-ion contribution in heat conductivity of solid gold*)
keisol[te_,ti_,x_]=alpha[x]*te*(1000/ti)^2/(1+B1[te,x]*(1000/ti))

(*electon heat conductivity of solid gold*)
ksol[te_,ti_,x_]=1/(1/keisol[te,ti,x]+1/kee[te,x])

(*parts of new formula for electron-ion contribution
 in electron heat conductivity of liquid gold*)
s[x_]=0.0363*Exp[0.4125*x]
t[x_]=0.7465*x-0.6244
z[x_]=8*10^(-4)/x/(1+0.4/x)

(*electron-ion contribution in heat conductivity of liquid gold*)
keiliq[te_,ti_,x_]=(s[x]+t[x]*Exp[-z[x]*ti])*te

(*electron heat conductivity of liquid gold*)
kliq[te_,ti_,x_]=1/(1/keiliq[te,ti,x]+1/kee[te,x])

(*full electron heat conductivity*)
k[te_,ti_,x_]=If[ti>Tm[x],kliq[te,ti,x],ksol[te,ti,x]]


(*Part VI*)

(*comparison with P.A. Zhilyaev QMD data*)
tZ[1]=11605
tZ[2]=23210
tZ[3]=34815
tZ[4]=46420
tZ[5]=58025
kZ[1]=439
kZ[2]=900
kZ[3]=1608
kZ[4]=1889
kZ[5]=2660
gZ=ListPlot[Table[{tZ[i],kZ[i]},{i,1,5}]]
gM=Plot[k[te,300,1],{te,10000,60000}]
Show[gZ,gM]
```

Appendix A.2. The second program "2T conduction"

```
(*the coefficients used here are taken from the work in
J.Phys.Conf.Ser. V.653, 012087 (Elbrus 2015)*)

t[r_,te_]=6*(te/11605)/(9.2*(r/19.5));

a=3.92; b=1.95; al=2*a+1;  be=a+1;  cab=(a-b)/(b+1);

yprime[r_]=((1+cab)*(r/19.3)^(al))/(1+cab*(r/19.3)^(be)) ;

cv[r_,te_]=131*t[r,te]*(1+3.07*t[r,te]*t[r,te])/(1+1.08*t[r,te]^2.07);

Trt=293; (*room temperature*)

xrt=19.28/19.5;

trt=Trt*6/(9.2*11605*(xrt^(2/3)));

(*electron-ion contribution in heat conductivity of solid gold*)
ksei[r_,te_,ti_]=
318*(r/19.3)*(yprime[r]/yprime[19.5])*Trt/ti*cv[r,te]/cv[19.5,298]

k0[r_,te_]=cv[r,te]

tl[ti_]=(ti-1337)/1000

xl[ti_]=0.887179-0.0328321*tl[ti]-0.0030982*(tl[ti]^2)-0.000164884*(tl[ti]^3)

tm=1337.0

xlm=xl[tm]

rl[ti_]=148.5+119.3*15.337*(ti/1000)/(14+ti/1000)

gam=2.

(*electron-ion contribution in heat conductivity of liquid gold*)
klei[r_,te_,ti_]=k0[r,te]*(3254/rl[ti])*((r/19.5)/xl[tm])
*(((r/19.5)/xl[ti])^gam)

(*electron-electron contribution in heat conductivity*)
keem[r_,te_]=
9.294*10^(-4)*t[r,te]/(1+0.03*Sqrt[t[r,te]]-0.2688*t[r,te]+

+0.9722*t[r,te]^2)*(r/19.5)^(-4./3.)

recks[r_,te_,ti_]=keem[r,te]+1/ksei[r,te,ti]
reckl[r_,te_,ti_]=keem[r,te]+1/klei[r,te,ti]
```

```
(*electron heat conductivity of solid (1) and liquid (2) gold *)
(*here "r" is density in g/cm^3 *)
ks[r_,te_,ti_]=1/recks[r,te,ti] (*1*)
kl[r_,te_,ti_]=1/reckl[r,te,ti] (*2*)
```

Appendix B. Limit of electron thermal transport

Heat flux j_q can be expressed in terms of the entropy flux j_s:

$$j_q = T_e j_s.$$

Taking into account that

$$T_e \mathrm{d}S = \mathrm{d}E - \mu \mathrm{d}N,$$

where S is the entropy, N is the number of particles, one connects the heat flux with the energy flux j_E and particle flux j_N:

$$j_q = T_e\, j_s = j_E - \mu\, j_N.$$

Here μ is a cheimical potential, close to the Fermi energy at not too high electron temperatures. Then integrating over all electrons within the conduction band with the energy of electron with the wave vector $\vec{k}$ equal to $\varepsilon(\vec{k})$ and velocity $v(\vec{k})$, we obtain

$$j_q = \int 2\frac{\mathrm{d}^3 k}{(2\pi)^3}(\varepsilon(\vec{k}) - \mu)v(\vec{k})f(\vec{k}).$$

Here $f(\vec{k})$ is the electron partition function. Then in the case of not too high temperatures, when $\varepsilon(\vec{k}) - \mu \simeq k_B T_e$ (only electrons within the energy interval $\sim k_B T_e$ are excited with their number $\sim n\, k_B T_e/\mu$), the maximum possible heat flux can be estimated as

$$j_q \simeq (k_B T_e)\,(n\, k_B T_e/\mu)\, v_{\mathrm{F}} \simeq (n\, \varepsilon_{\mathrm{F}})\,(k_B T_e/\mu)^2\, v_{\mathrm{F}},$$

where v_{F} being the Fermi velocity.

References
[1] Milchberg H M, Freeman R R, Davey S C and More R M 1988 *Phys. Rev. Lett.* **61** 2364–2367
[2] Ng A, Celliers P, Forsman A, More R M, Lee Y T, Perrot F, Dharma-Wardana M W C and Rinker G A 1994 *Phys. Rev. Lett.* **72** 3351–3354
[3] Komarov P S, Ashitkov S I, Ovchinnikov A V, Sitnikov D S, Veysman M E, Levashov P R, Povarnitsyn M E, Agranat M B, Andreev N E, Khishchenko K V and Fortov V E 2009 *J. Phys. A: Math. Theor.* **42** 214057
[4] Veysman M E, Agranat M B, Andreev N E, Ashitkov S I, Fortov V E, Khishchenko K V, Kostenko O F, Levashov P R, Ovchinnikov A V and Sitnikov D S 2008 *J. Phys. B: At. Mol. Opt. Phys.* **41** 125704
[5] Agranat M B, Andreev N E, Ashitkov S I, Veysman M E, Levashov P R, Ovchinnikov A V, Sitnikov D S, Fortov V E and Khishchenko K V 2007 *JETP Lett.* **85** 271–276
[6] Zhakhovskii V V and Inogamov N A 2010 *JETP Lett.* **92** 521–526
[7] Ashitkov S I, Agranat M B, Kanel' G I, Komarov P S and Fortov V E 2010 *JETP Lett.* **92** 516–520
[8] Inogamov N, Zhakhovsky V V, Khokhlov V A and Shepelev V V 2011 *JETP Lett.* **93** 226–232
[9] Krasyuk I K, Pashinin P P, Semenov A Y, Khishchenko K V and Fortov V E 2016 *Laser Phys.* **26** 094001
[10] Anisimov S I, Zhakhovskii V V, Inogamov N A, Nishihara K, Oparin A M and Petrov Yu V 2003 *JETP Lett.* **77** 606–610
[11] Ivanov D S and Zhigilei L V 2003 *Phys. Rev. B* **68** 064114
[12] Inogamov N A, Zhakhovskii V V, Ashitkov S I, Khokhlov V A, Shepelev V V, Komarov P S, Ovchinnikov A V, Sitnikov D S, Petrov Yu V, Agranat M B, Anisimov S I and Fortov V E 2011 *Contrib. Plasma Phys.* **51** 367–374
[13] Demaske B J, Zhakhovsky V V, Inogamov N A and Oleynik I I 2010 *Phys. Rev. B* **82** 064113
[14] Zhakhovskii V V, Nishihara K, Anisimov S I and Inogamov N A 2000 *JETP Lett.* **71** 167–172

[15] Upadhyay A K, Inogamov N A, Rethfeld B and Urbassek H 2008 *Phys. Rev.* B **78** 045437
[16] Inogamov N A, Zhakhovskii V V and Khokhlov V A 2015 *J. Exp. Theor. Phys.* **120** 15–48
[17] Inogamov N A, Zhakhovsky V V, Hasegawa N, Nishikino M, Yamagiwa M, Ishino M, Agranat M B, Ashitkov S I, Faenov A Ya, Khokhlov V A, Ilnitsky D K, Pikuz T A, Takayoshi S, Tomita T and Kawachi T 2015 *Appl. Phys.* B **119** 413–419
[18] Inogamov N A, Anisimov S I and Retfeld B 1999 *J. Exp. Theor. Phys.* **88** 1143–1150
[19] Anisimov S I, Inogamov N A, Oparin A M, Rethfeld B, Yabe T, Ogawa M and Fortov V E 1999 *Appl. Phys.* A **69** 617–620
[20] Povarnitsyn M E, Itina T E, Sentis M, Khishchenko K V and Levashov P R 2007 *Phys. Rev.* B **75** 235414
[21] Inogamov N A, Zhakhovskii V V, Ashitkov S I, Petrov Yu V, Agranat M B, Anisimov S I, Nishihara K and Fortov V E 2008 *J. Exp. Theor. Phys.* **107** 1–19
[22] Inogamov N A, Zhakhovsky V V, Khokhlov V A, Demaske B J, Khishchenko K V and Oleynik I I 2014 *J. Phys.: Conf. Ser.* **500** 192023
[23] Ilnitsky D K, Khokhlov V A, Inogamov N A, Zhakhovsky V V, Petrov Yu V, Khishchenko K V, Migdal K P and Anisimov S I 2014 *J. Phys.: Conf. Ser.* **500** 032021
[24] Starikov S V and Pisarev V V 2015 *J. Appl. Phys.* **117** 135901
[25] Starikov S V, Faenov A Y, Pikuz T A, Skobelev I Y, Fortov V E, Tamotsu S, Ishino M, Tanaka M, Hasegawa N, Nishikino M, Kaihori T, Imazono T, Kando M and Kawachi T 2014 *Appl. Phys.* B **116** 1005–1016
[26] Norman G, Starikov S, Stegailov V, Fortov V, Skobelev I, Pikuz T, Faenov A, Tamotsu S, Kato Y, Ishino M, Tanaka M, Hasegawa N, Nishikino M, Ohba T, Kaihori T, Ochi Y, Imazono T, Fukuda Y, Kando M and Kawachi T 2012 *J. Appl. Phys.* **112** 013104
[27] Lin Z, Zhigilei L V and Celli V 2008 *Phys. Rev.* B **77** 075133
[28] Petrov Yu V, Inogamov N A and Migdal K P 2013 *JETP Lett.* **97** 20–27
[29] Chen Z, Holst B, Kirkwood S E, Sametoglu V, Reid M, Tsui Y Y, Recoules V and Ng A 2013 *Phys. Rev. Lett.* **110** 135001
[30] Petrov Yu V, Migdal K P, Inogamov N A and Zhakhovsky V V 2015 *Applied Physics B* **119** 401–411
[31] Hohlfeld J, Wellershoff S S, Guedde J, Conrad U, Jaehnke V and Matthias E 2000 *Chem. Phys.* **251** 237–258
[32] Migdal K P, Il'nitsky D K, Petrov Yu V and Inogamov N A 2015 *J. Phys.: Conf. Ser.* **653** 012086
[33] Petrov Yu V, Inogamov N A, Anisimov S I, Migdal K P, Khokhlov V A and Khishchenko K V 2015 *J. Phys.: Conf. Ser.* **653** 012087
[34] Petrov Yu V, Inogamov N A and Migdal K P 2015 *PIERS Proceedings* pp 2431–2435
[35] Graf M J, Greeff C W and Boettger J C 2004 *AIP Conf. Proc.* **706** 65–68
[36] Khishchenko K V 2008 *J. Phys.: Conf. Ser.* **98** 032023
[37] Khishchenko K V 2008 *J. Phys.: Conf. Ser.* **121** 022025
[38] Levashov P R and Khishchenko K V 2007 *AIP Conf. Proc.* **955** 59–62
[39] Inogamov N A, Petrov Yu V, Zhakhovsky V V, Khokhlov V A, Demaske B J, Ashitkov S I, Khishchenko K V, Migdal K P, Agranat M B, Anisimov S I, Fortov V E and Oleynik I I 2012 *AIP Conf. Proc.* **1464** 593–608
[40] Inogamov N A, Khokhlov V A, Zhakhovsky V V, Petrov Yu V, Khishchenko K V and Anisimov S I 2015 *PIERS Proceedings* pp 2422–2426
[41] Widmann K, Ao T, Foord M E, Price D F, Ellis A D, Springer P T and Ng A 2004 *Phys. Rev. Lett.* **92** 125002
[42] Ao T, Ping Y, Widmann K, Price D F, Lee E, Tam H, Springer P T and Ng A 2006 *Phys. Rev. Lett.* **96** 055001
[43] Ping Y, Hanson D, Koslow I, Ogitsu T, Prendergast D, Schwegler E, Collins G and Ng A 2006 *Phys. Rev. Lett.* **96** 255003
[44] Ping Y, Hanson D, Koslow I, Ogitsu T, Prendergast D, Schwegler E, Collins G and Ng A 2008 *Phys. Plasmas* **15** 056303
[45] Chen Z, Sametoglu V, Tsui Y Y, Ao T and Ng A 2012 *Phys. Rev. Lett.* **108** 165001
[46] Fourment C, Deneuville F, Descamps D, Dorchies F, Petit S and Peyrusse O 2014 *Phys. Rev.* B **89** 161110(R)
[47] Ashitkov S I, Komarov P S, Struleva E V, Agranat M B and Kanel G I 2015 *JETP Lett.* **101** 276–281
[48] Kresse G and Furthmuller J 1996 *Comput. Mater. Sci.* **6** 15
[49] Levashov P R, Sin'ko G V, Smirnov N A, Minakov D V, Shemyakin O P and Khishchenko K V 2010 *J. Phys.: Condens. Matter* **22** 505501
[50] Sin'ko G V, Smirnov N A, Ovechkin A A, Levashov P R and Khishchenko K V 2013 *High Energy Density Phys.* **9** 309–314
[51] Minakov D V, Levashov P R, Khishchenko K V and Fortov V E 2014 *J. Appl. Phys.* **115** 223512
[52] Inogamov N A and Petrov Yu V 2010 *J. Exp. Theor. Phys.* **110** 446–468